



Article (refereed) – Published version

Serpelloni, Enrico; Faccenna, Claudio; Spada, Giorgio; Dong, Danan; Williams, Simon D.P.. 2013 Vertical GPS ground motion rates in the Euro-Mediterranean region: New evidence of velocity gradients at different spatial scales along the Nubia-Eurasia plate boundary. *Journal of Geophysical Research: Solid Earth*, 118 (11). 6003-6024. [10.1002/2013JB010102](https://doi.org/10.1002/2013JB010102)

This version available at <http://nora.nerc.ac.uk/504446/>

NERC has developed NORA to enable users to access research outputs wholly or partially funded by NERC. Copyright and other rights for material on this site are retained by the rights owners. Users should read the terms and conditions of use of this material at <http://nora.nerc.ac.uk/policies.html#access>

AGU Publisher statement: An edited version of this paper was published by AGU. Copyright (2013) American Geophysical Union. Further reproduction or electronic distribution is not permitted.

Serpelloni, Enrico; Faccenna, Claudio; Spada, Giorgio; Dong, Danan; Williams, Simon D.P.. 2013 Vertical GPS ground motion rates in the Euro-Mediterranean region: New evidence of velocity gradients at different spatial scales along the Nubia-Eurasia plate boundary. *Journal of Geophysical Research: Solid Earth*, 118 (11). 6003-6024. [10.1002/2013JB010102](https://doi.org/10.1002/2013JB010102)

To view the published open abstract, go to <http://dx.doi.org/10.1002/2013JB010102>

Contact NOC NORA team at
publications@noc.soton.ac.uk

Vertical GPS ground motion rates in the Euro-Mediterranean region: New evidence of velocity gradients at different spatial scales along the Nubia-Eurasia plate boundary

Enrico Serpelloni,¹ Claudio Faccenna,² Giorgio Spada,³ Danan Dong,⁴ and Simon D. P. Williams⁵

Received 1 February 2013; revised 4 October 2013; accepted 14 October 2013; published 19 November 2013.

[1] We use 2.5 to 14 years long position time series from >800 continuous Global Positioning System (GPS) stations to study vertical deformation rates in the Euro-Mediterranean region. We estimate and remove common mode errors in position time series using a principal component analysis, obtaining a significant gain in the signal-to-noise ratio of the displacements data. Following the results of a maximum likelihood estimation analysis, which gives a mean spectral index ~ -0.7 , we adopt a power law + white noise stochastic model in estimating the final vertical rates and find 95% of the velocities within ± 2 mm/yr, with uncertainties from filtered time series $\sim 40\%$ smaller than from the unfiltered ones. We highlight the presence of statistically significant velocity gradients where the stations density is higher. We find undulations of the vertical velocity field at different spatial scales both in tectonically active regions, like eastern Alps, Apennines, and eastern Mediterranean, and in regions characterized by a low or negligible tectonic activity, like central Iberia and western Alps. A correlation between smooth vertical velocities and topographic features is apparent in many sectors of the study area. Glacial isostatic adjustment and weathering processes do not completely explain the measured rates, and a combination of active tectonics and deep-seated geodynamic processes must be invoked. Excluding areas where localized processes are likely, or where subduction processes may be active, mantle dynamics is the most likely process, but regional mantle modeling is required for a better understanding.

Citation: Serpelloni, E., C. Faccenna, G. Spada, D. Dong, and S. D. P. Williams (2013), Vertical GPS ground motion rates in the Euro-Mediterranean region: New evidence of velocity gradients at different spatial scales along the Nubia-Eurasia plate boundary, *J. Geophys. Res. Solid Earth*, 118, 6003–6024, doi:10.1002/2013JB010102.

1. Introduction

[2] The vertical component of the Earth's surface velocity field is important to constrain dynamic models of lithospheric loading, deep-seated geodynamics, active tectonics, and magmatic and hydrologic processes. In addition, assessing vertical ground displacement rates is crucial to determine relative sea level variations, which are paramount for coastal hazard assessment. However, while for more than a decade, GPS has been widely used for measuring horizontal

deformations with excellent precisions, the use of vertical GPS deformation constitutes a challenge.

[3] The precision of vertical positions determined by GPS is typically about 3–5 times lower than for the horizontal [e.g., Bennett *et al.*, 2007], due to various reasons. Moreover, GPS measurements of vertical surface motion are susceptible to numerous potential errors, besides the geometric weaknesses in the height component of GPS in general. These derive from delays associated with tropospheric water vapor, unmodeled phase delays, mismodeled satellite orbital motions, variations in ground-based antenna phase centers, different loading processes, monument instability, and others [e.g., van Dam *et al.*, 1994, 2001; Blewitt and Lavallee, 2002; King and Williams, 2009; Petrie *et al.*, 2010; King *et al.*, 2012]. Furthermore, biases and inconsistencies in the reference frame and satellite orbits, or in the processing strategy, propagate into the vertical component. This increases the noise level and introduces artificial long-term trends and/or common systematic variations, correlated over large areas or continental regions [e.g., Wdowinski *et al.*, 1997; Johansson *et al.*, 2002; Dong *et al.*, 2006; Kierulf *et al.*, 2008; Fay *et al.*, 2008].

[4] Since stations heights and height changes as observed by GPS are related to a global reference frame, the result is

Additional supporting information may be found in the online version of this article.

¹Istituto Nazionale di Geofisica e Vulcanologia, Centro Nazionale Terremoti, Bologna, Italy.

²Dipartimento di Scienze, Università di Roma III, Rome, Italy.

³Dipartimento di Scienze di Base e Fondamenti, Università di Urbino Carlo Bo, Urbino, Italy.

⁴Eastern China Normal University, Shanghai, China.

⁵National Oceanography Centre, Liverpool, UK.

Corresponding author: E. Serpelloni, Istituto Nazionale di Geofisica e Vulcanologia, Centro Nazionale Terremoti, Via D. Creti 12, IT-40128 Bologna, Italy. (enrico.serpelloni@bo.ingv.it)

always directly affected by the realization and stability of this frame, especially by possible variations of the coordinate origin with respect to the Earth's crust. Differences between different International Terrestrial Reference Frame (ITRF) releases suggest that the geocenter may drift along the Z axis [Argus, 2007; Altamimi et al., 2007], although the agreement between ITRF2008 and ITRF2005 points to an imprecise ITRF2000 origin [Altamimi et al., 2011]. Hence, the measured ITRF vertical rates might be slightly biased, with the bias evolving with latitude, and uplift and subsidence are not absolute, being possibly shifted in location, thus making the interpretation of vertical rates difficult, particularly when rates are small.

[5] With the exception of areas subject to natural or anthropogenic subsidence, vertical velocities are typically smaller by an order of magnitude compared to the horizontal ones (i.e., they are in the mm/yr range in a global reference frame). Global and regional sea level studies, also, require the highest accuracies [e.g., Church et al., 2001]. Consequently, vertical velocities at GPS stations need to be determined with sub-millimeter/yr accuracies [Kaniuth and Vetter, 2005; Bennett and Hreinsdóttir, 2007; Kierulf et al., 2008; Bouin and Wöppelmann, 2010]. Reliable information on the equipment used and antenna mounting, as well as the realization of a stable and consistent global geocentric reference frame, is mandatory to obtain vertical GPS position time series useful for geophysical interpretations. Any change in the equipment, in the geocentric datum and in the parameterization or in the models used to analyze the GPS data might indeed affect the vertical velocity [e.g., Williams, 2003; Steigenberger et al., 2006].

[6] While horizontal GPS velocities have been extensively used to constrain plate kinematics, geodynamics, and active tectonics along the Nubia-Eurasia plate boundary in the Euro-Mediterranean region [e.g., Faccenna and Becker, 2010; Floyd et al., 2010; Serpelloni et al., 2007], the use of vertical GPS rates is still limited to coastal stations for sea level studies, at both continental [e.g., Becker et al., 2002; Teferle et al., 2008; Bouin and Wöppelmann, 2010; Ostancaux et al., 2012] and regional scales [e.g., Bennett and Hreinsdóttir, 2007; Buble et al., 2010; Anzidei et al., 2011], postglacial rebound [e.g., Johansson et al., 2002; Nocquet et al., 2005], local anthropogenic or natural subsidence [e.g., Baldi et al., 2009], and volcano research and monitoring [e.g., Bonaccorso et al., 2006]. Dense regional GPS vertical velocity fields [e.g., Devoti et al., 2010, 2011; Bennett et al., 2012] have recently provided new images of rather coherent vertical velocity patterns at different spatial scales, which can be interpreted in terms of geodynamic processes.

[7] Despite the increasing importance of vertical deformation data, a synoptic view of vertical ground motion rates at the scale of the Nubia-Eurasia plate boundary, including continental areas of the Euro-Mediterranean region, is still missing and this is the goal of the present work. The development of new continuous GPS (or more generally Global Navigation Satellite System, GNSS) networks, realized for diverse purposes (including geodesy, navigation, topography, and geophysics) provides increasingly detailed information on the three-dimensional velocities. Here we present results obtained from the analysis of data from >1200 continuous GPS (cGPS) stations between longitudes -15°E and 39°E and latitudes 28°N and 59°N , with >800 sites having time series longer than 2.5 years. We perform a

homogeneous reanalysis of the entire data set from January 1998 to April 2011 and provide a self-consistent velocity solution for >800 stations. During this interval, precise orbits have been realized within the "IGS Repro 1" campaign (<http://acc.igs.org/reprocess.html>) and are consistent with the absolute phase center model IGS05. After 16 April 2011, instead, precise orbits are obtained adopting the IGS08 phase center model, and self-consistent orbits for the entire observation time span used in this work will be available after the "IGS Repro 2" reprocessing campaign (<http://acc.igs.org/reprocess2.html>).

[8] We present our velocities in a global reference frame obtained by aligning daily loosely constrained solutions to the IGS realization of the ITRF2008, which has been shown to be far more accurate than previous ITRF solutions [Altamimi et al., 2011]. To determine the secular change of the station position with the highest accuracies and provide realistic uncertainties, we adopt a time series analysis strategy that incorporates a principal component analysis (PCA) procedure to estimate spatially correlated common mode error (CME), and estimates of realistic uncertainties using a maximum likelihood estimation (MLE) optimization scheme.

[9] The paper is organized as follows: section 2 describes the GPS/GNSS stations available, section 3 describes the data processing and postprocessing steps, section 4 describes the general features of the vertical velocity field, section 5 provides estimates for the glacial isostatic adjustment (GIA) component of the vertical velocity field in the study region, and section 6 describes velocity gradients at specific cross sections along the Africa-Eurasia plate boundary and discuss the major geodynamic implications of the estimated velocity field.

2. Continuous GPS Networks

[10] We use raw GPS data, obtained from several continuously operating networks in the Euro-Mediterranean and African regions. Table S1 in the supporting information lists the networks used in this work and Figure 1 shows the distribution of stations, with symbols colored according to the length of the time series. In Figure 1 we classify the cGPS networks into three main categories: geophysical, geodetic, and topographic. This is just a formal categorization, based on the main purposes of each network, regardless of the quality of the single station monuments. However, since most of the geodetic networks analyzed do not provide log files or pictures of the monuments, it is difficult to further detail this classification, which is still in progress.

[11] The distribution of GPS stations is not uniform around the Mediterranean basin, with the majority of stations located in its northern side, with the exception of the Middle East (Israel). Station density is sparse in central and northern Europe and significantly dense in Spain, southern France, and Italy. The reasons are (i) our GPS solution does not include all of the continuous networks available north of the Alpine region (e.g., the Réseau GNSS Permanent network in France is missing), (ii) some cGPS data are not open to public, and/or (iii) the length of the time series are still too short (Figure 1).

3. GPS Data Analysis

[12] Vertical velocities are obtained adopting a three-step approach, including (1) raw phase data reduction, (2)

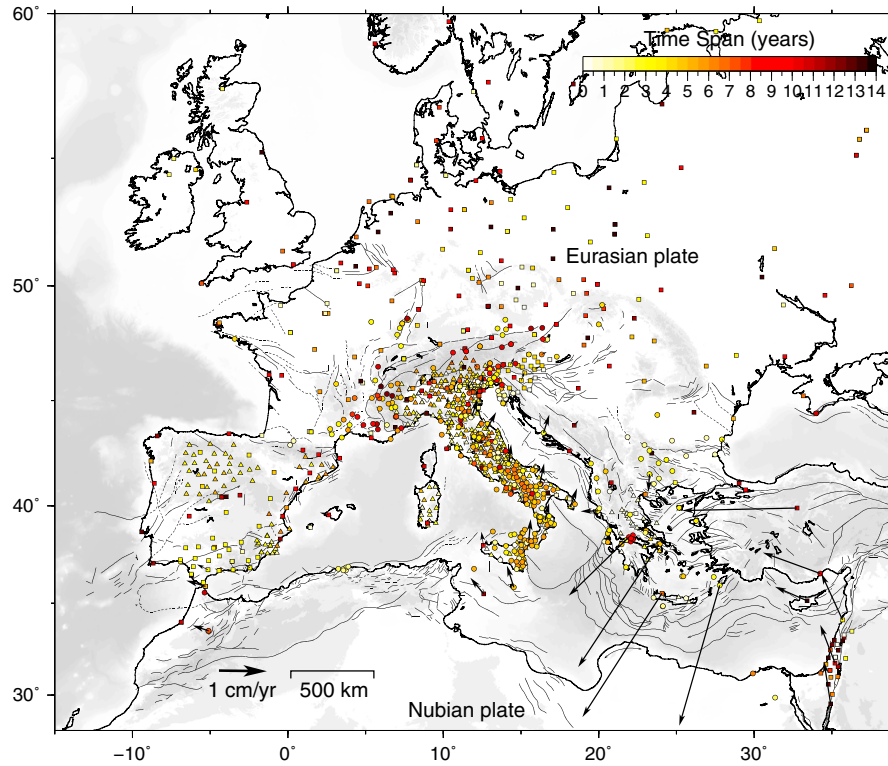


Figure 1. Distribution of the continuous GPS (cGPS) stations used in this work. Circles show geophysical stations, built specifically for monitoring crustal deformation, and where the highest monument and data quality are expected. Squares show geodetic stations, built to estimate and maintain global or regional reference frames, and where the highest attention to data quality and continuity through time are expected. Triangles show topographic stations, built to provide data for navigation or cadastral purposes, and where both monument and the data quality are not restrictive realization criteria. Symbols are colored based on the length of the data span for each station. The black arrows show horizontal velocities, with respect to a fixed Eurasian frame, for a few representative stations on different domains of the Nubia-Eurasia plate boundary zone.

combination of loosely constrained solutions and reference frame definition, and (3) time series analysis [Serpelloni *et al.*, 2006, 2010].

[13] In the first step, we use daily GPS phase observations to estimate site position, adjustments to satellite orbital parameters and time-variable piecewise linear zenith and horizontal gradient tropospheric delay parameters by means of the GAMIT (V10.4) software [Herring *et al.*, 2010], applying loose constraints to geodetic parameters. Each network (see Table S1) is analyzed individually, with the exception of those with >40 stations, which are divided into smaller subnetworks, following a simple geographic criterion, while maintaining the shortest baselines as possible. We used orbital solutions from Scripps Orbit and Permanent Array Center (SOPAC), obtained in a homogeneous reanalysis of the global data set, but allowed these orbital solutions to relax so as to promote the consistency of our solutions for the daily network polyhedron and the overall geometrical consistency with SOPAC solutions in the combination step. GPS phase data are weighted according to an elevation-angle-dependent error model [Herring *et al.*, 2010] using an iterative analysis procedure whereby the elevation dependence is determined from the observed scatter of phase residuals. We apply the ocean loading and a pole-tide correction model FES2004 [Lyard *et al.*, 2006]. We use the Global Mapping Function (GMF) [Boehm *et al.*, 2006] for both hydrostatic and

nonhydrostatic components of the tropospheric delay model and the global pressure and temperature model. We test the use of the Vienna Mapping Function (VMF1) [Boehm and Schuh, 2004], which is the most accurate mapping function globally available at present, on a regional subnetwork and find no significant differences in terms of velocities and uncertainties with respect to the results obtained using the GMF. Here we use the GMF mapping function in order to maintain consistency with solutions of the IGS network provided by SOPAC. We use the IGS absolute antenna phase center model for both satellite and ground-based antennas, which improves the accuracy of estimates for the vertical components of site position by mitigating reference frame scale and atmospheric mapping function errors [e.g., Schmid *et al.*, 2005, 2007]. Loosely constrained solutions are stored in the form of ASCII GAMIT H-files and SINEX files and contribute to the Istituto Nazionale di Geofisica e Vulcanologia (INGV) combined solution [Avallone *et al.*, 2010; Devoti *et al.*, 2010].

[14] In the second step we use the ST_FILTER program of the QOCA software, which adopts a Kalman filter estimation algorithm [Dong *et al.*, 1998, 2002], to combine our daily loosely constrained solutions with the global solutions made available by SOPAC (<http://sopac.ucsd.edu>), and simultaneously realize a global reference frame by applying generalized constraints [Dong *et al.*, 1998]. Specifically, we define

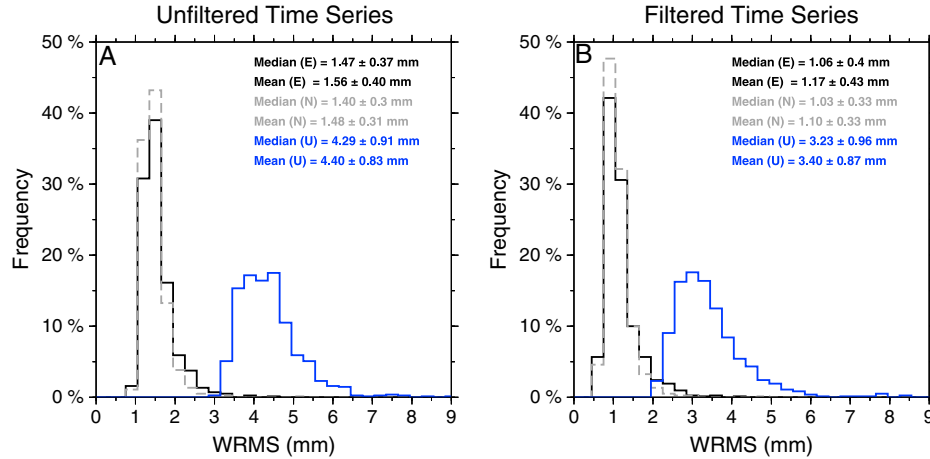


Figure 2. Distribution of WRMS values for the E, N, and Up components of the (a) unfiltered and (b) filtered residual time series (see section 3.1). The uncertainty associated with the mean values is 1σ , whereas the uncertainty associated with the median values is the interquartile range (IQR).

the reference frame by minimizing coordinates and velocities of the IGS global core stations (<http://igsceb.jpl.nasa.gov>), while estimating a seven-parameter transformation with respect to the IGS realization of the ITRF2008 NNR frame [Altamimi *et al.*, 2011]. In defining the reference frame, we account for seasonal motions of IGS core sites.

[15] In the third step, we analyze the absolute IGS08 position time series in order to estimate the tridimensional velocities. Changes in stations positions are modeled using the following functional model:

$$x(t) = x_0 + bt + \alpha \cdot \sin(\omega t + \varphi) + \sum_{j=1}^n \Delta x_j H(t - t_j), \quad (1)$$

where x is the position of a point, t is the time, x_0 is the initial position bias, b is the secular rate, α and φ are the amplitude and phase of the annual and semiannual seasonal signals, respectively, and H is the Heaviside step function defining coordinate jumps (Δx) at a given time t_j . Only stations having a minimum length of 2.5 years are retained in this and subsequent analyses, to avoid biases due to unreliable estimated seasonal signals [Blewitt and Lavallee, 2002] and underestimated velocity uncertainties due to absorbed correlated noise content in estimated trends of short time series [Williams *et al.*, 2004; Bos *et al.*, 2009].

[16] During the observation time span, a few stations recorded significant coseismic offsets due to the 2008 M_w 6.4 Achaia (Greece) earthquake [Ganas *et al.*, 2009], the 2009 M_w 6.3 L'Aquila (Italy) earthquake [Serpelloni *et al.*, 2012a], and the 2011 M_w 5.1 Lorca (Spain) earthquake. Coseismic offsets are modeled with a Heaviside step function. For the 2009 L'Aquila earthquake, we model the postseismic deformation estimating the amplitude of an exponential decay function, adopting decay times derived in Devoti *et al.* [2012]. Nontectonic jumps, mainly due to changes in the stations equipment, are defined from the analysis of station log files, when available, and from visual inspections of the time series. Outliers are cleaned adopting a postfit root-mean-square (RMS) criterion, in particular, we discard values larger than three times the postfit weighted root-mean-square (WRMS). Figure 2 shows frequency

histograms of WRMS values for the horizontal and vertical components of the 826 stations considered in this work. The mean vertical WRMS value is about three times larger than the horizontal ones. The residual time series obtained by estimating and removing from the absolute IGS08 time series the linear velocity, instrumental offsets, seasonal terms and, eventually, coseismic and postseismic transients, are used in the subsequent analyses.

3.1. Filtering of Common Mode Errors

[17] Residual time series contain various systematic errors (from network common to site dependent) and random errors, as well as unmodeled signals. In regional network analysis, the so-called common mode error (CME) is one of the major spatially correlated error sources in GPS solutions, which is mitigated through a technique commonly referred to as regional filtering. This was first introduced by Wdowinski *et al.* [1997] by removing a common mode bias from each coordinate components computed by “stacking” the position residuals of the stations and estimating and removing the mean value. This approach assumes that the CME is spatially uniform, which is a good approximation for networks of hundreds of kilometers extent, but as the spatial extent increases, as in the case of the network analyzed in the present work, the assumption is no longer valid and the common mode bias becomes progressively smaller [e.g., Marquez-Azua and Demets, 2003]. Dong *et al.* [2006] adopted a PCA technique, which decomposes the network time series into a set of temporally varying (principal component) modes, where each mode consists of a common temporal function and related different spatial response, providing a mathematical framework to perform spatiotemporal filtering, removing the assumption of spatially uniform distribution, and letting the data themselves reveal the spatial distribution of the CME.

[18] Here we apply the PCA method of Dong *et al.* [2006] to filter the position time series with the goal of reducing the daily scatter, allowing for more accurate determinations of the time series parameters in equation (1). In this step we first discard stations affected by significant local effects, which are identified looking at sites with the highest WRMS values,

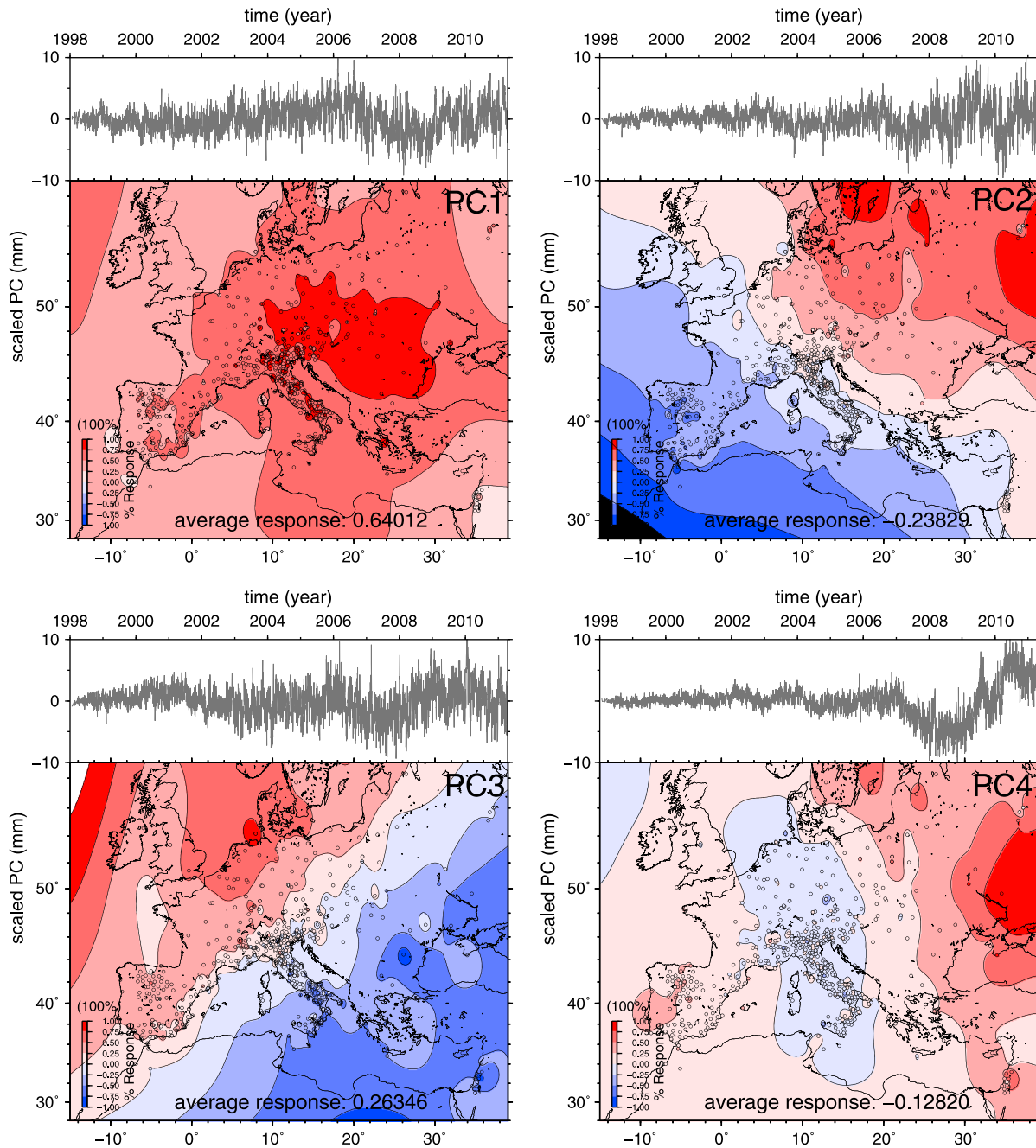


Figure 3. Temporal and spatial response of the first four PCs of the vertical component. (top) The scaled PC and (bottom) its normalized spatial eigenvectors. Red and blue colors represent positive and negative response to the scaled PC, respectively. Color contours of the normalized spatial response are derived from smoothing spline fits to the discrete values at each site. Similar figures for the E and N components are given in Figures S1 and S2, respectively.

by visual inspection of the time series. Moreover, stations affected by strong local effects (including possible unaccounted offsets) show anomalously large spatial response, in contrast with nearly uniform lower response of the rest of stations. We discard stations with a number of daily solutions $< 20\%$ of the total daily solutions expected in the examined time interval. We also discard all epochs for which the number of stations is $< 5\%$ than the total number of stations. After this selection, the PCA is performed using 642 out of the 826 stations and 4723 epochs.

[19] Following *Dong et al.* [2006], the output of PCA, i.e., the principal components (PCs) and the spatial eigenvectors, can be used to perform the regional filtering correction of GPS time series. The PCA decomposition is based on a criterion of pattern power, i.e., the pattern with the biggest power is the first PC, and so on for subsequent PCs. The eigenvalues of the east, north, and vertical covariance matrix represent the share of each PC mode in the total covariance. The cumulated shares for the first 30 PCs are displayed in Figure S1 of the supporting information. It is worth noting that for the larger

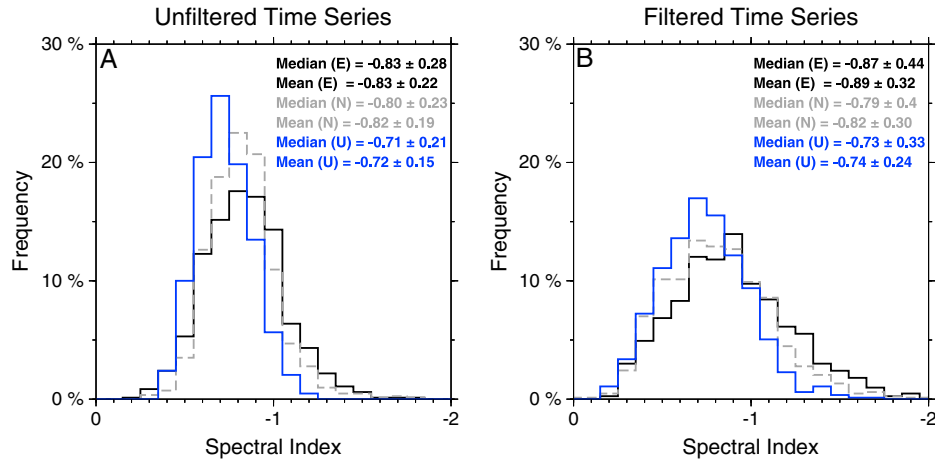


Figure 4. Distribution of the spectral index (κ) estimated from MLE analysis for the E, N, and Up components from (a) unfiltered and (b) filtered time series. The uncertainty associated with the mean values is 1σ , whereas the uncertainty associated with the median values is the IQR.

and less homogeneous network used in this work, comparing to the SCIGN network in southern California analyzed in *Dong et al.* [2006], the power of the “common mode error” spreads into several PCs due to limited wavelength and larger complexity of the CME patterns. The first PC eigenvalues of the horizontal components show higher percentages than the vertical one (Figure S1), and the “power” of first PCs in our work is significantly lower than that in *Dong et al.* [2006]. Accordingly, the criteria of the PC modes assumed as the CME representation should be modified since a single PC is no longer able to reflect the whole spatial and temporal patterns of the CME.

[20] In *Dong et al.* [2006], a PC mode is considered as “common mode” if most of the sites ($>50\%$) have a significant normalized response ($>25\%$), and the eigenvalues of this mode exceed 1% of the sum of all eigenvalues. Thus, only the top few PC modes are potential candidates for the common mode, and higher-order modes are related to a few stations and reflect local effects. In *Dong et al.* [2006], these criteria only fit the first PC, which is then used to perform the regional filtering. Figure 3 shows the spatial and temporal response of the first four PCs for the vertical position time series (the same for the east and north components are given in Figures S2 and S3). PCA performed for Italy and the surroundings (between longitude $3\text{--}22^\circ\text{E}$ and latitude $34\text{--}50^\circ\text{N}$), for the Mediterranean basin (between longitude $10\text{--}39^\circ\text{W}$ and latitude $29\text{--}51^\circ\text{N}$), and for the Euro-Mediterranean area (between longitude $15\text{--}39^\circ\text{W}$ and latitude $28\text{--}60^\circ\text{N}$) provides different spatial and temporal patterns of the first PC, suggesting that the wavelength of the CME is not so long and it is likely “diluted” into several PCs, which is also suggested by Figure S1.

[21] Figure 3 shows that the first principal component (PC1) is close to spatially uniformly distributed, likely representing the “common” or mean part of the CME, with the subsequent PCs representing the remaining modifications of the CME. PC2 shows a SW-NE smoothed transition pattern, which looks like “common,” not showing local effects from a few stations. A similar smoothed pattern, but oriented NE-SW, is observed for PC3. PC4, instead, shows a “group” pattern, with a few stations having strong amplitudes,

indicating that this PC mode probably has both “local” and “common” patterns. Subsequent PCs, not shown here, predominantly show local effects. For the horizontal components (Figures S1 and S2), we observe similar patterns, with a spatially uniform response of PC1 and smoothed transitions for PC2 and PC3.

[22] Since the CME in the study region is not likely a very long wavelength common pattern (although its nature is still unknown) and that higher-order PCs have a comprehensively small power (powers of the first four PCs are 42%, 6%, 5%, and 1% of the total power; see Figure S3), so that it is easy to be mixed with the local effects, the high-order PCs must not be used for regional filtering. Here we use the first three PCs to perform regional filtering. For cGPS stations used in the PCA, we use their responses to calculate the CME correction, whereas for stations excluded from the PCA (because of big gaps, strong local effects, or sparse data), we use the average response to calculate their CME corrections.

[23] The space-time filtering significantly reduces the scattering of the position and, as a result, after removing the CME, the typical repeatability in our analysis is ~ 1 mm for the horizontal components, and ~ 3 mm for vertical component (see Figure 2). In particular, for the vertical component, we obtain a 30% gain in the daily repeatability, significantly improving the signal to noise ratio. Figure S4 shows an example of raw time series (with linear trend and seasonal signals) before and after regional spatial filtering. Reducing the scatter of the original time series makes, for example, the pattern of seasonal variations usually better defined, although we do not find significant changes in the amplitudes of the annual signal and semiannual signals (see Figure S5).

[24] Filtering of CME significantly improves the precision of our vertical velocity estimates but may affect the velocity estimates. We evaluate these changes by comparing horizontal and vertical velocities, estimated assuming the presence of white noise only, from the unfiltered and filtered time series. We find that 95% of horizontal velocity differences from unfiltered and filtered time series are between ± 0.2 mm/yr, whereas 95% vertical rates differences are within ± 0.4 mm/yr. The larger differences are observed for stations with shorter time spans where the regional filtering improves the velocity

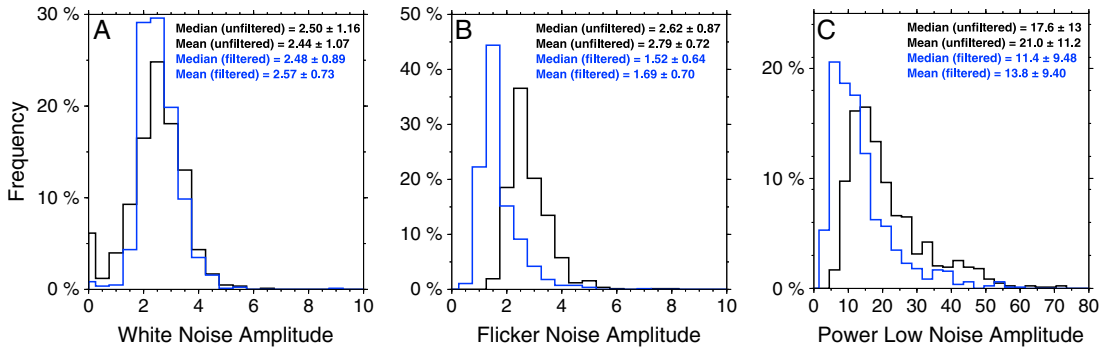


Figure 5. Distribution of the (a) WN, (b) FN, and (c) PL noise amplitudes estimated from MLE analysis for the vertical component for unfiltered (black line) and filtered (blue line) time series. The uncertainty associated with the mean values is 1σ , whereas the uncertainty associated with the median values is the IQR.

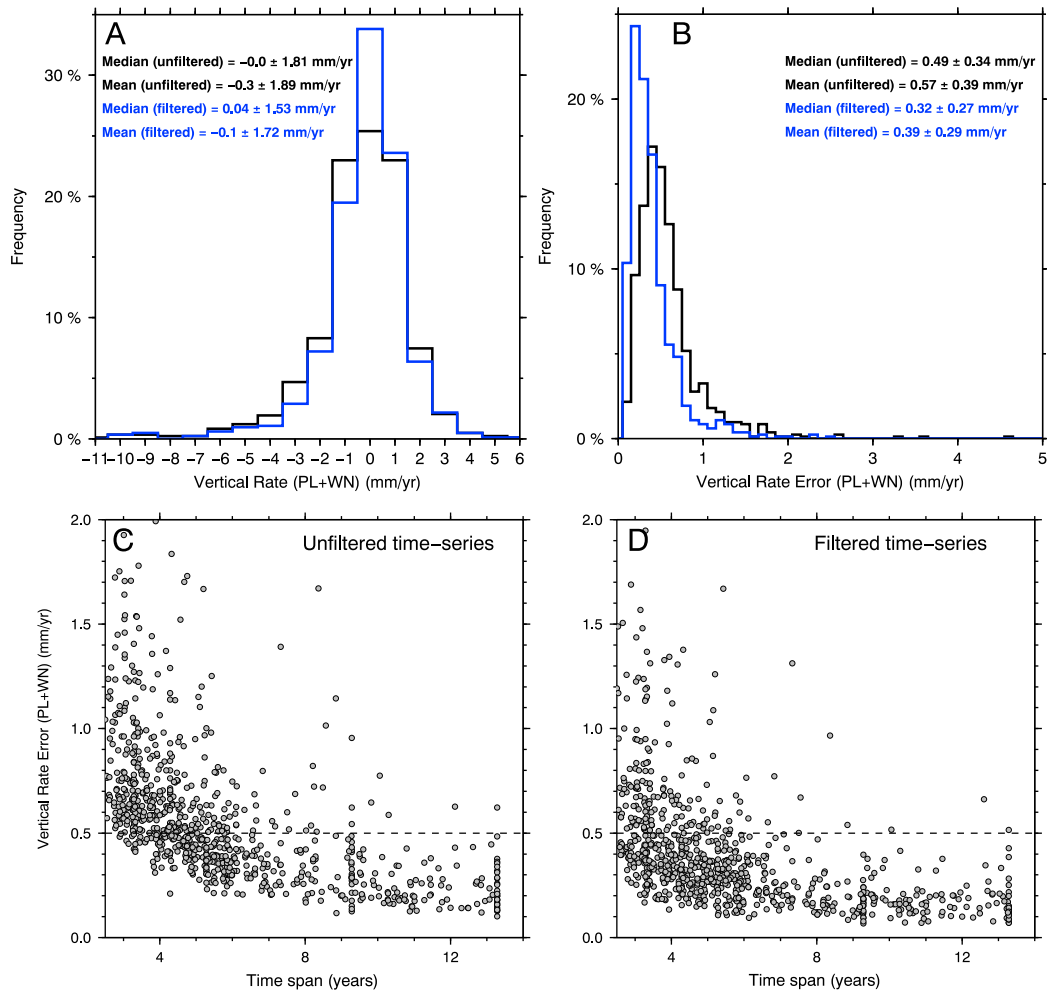


Figure 6. (a) Distribution of vertical velocity values estimated assuming a PL + WN noise model from unfiltered (black line) and filtered (blue line) time series. (b) Histogram of the distribution of vertical velocity uncertainties estimated from a PL + WN model from unfiltered (black line) and filtered (blue line) time series. The uncertainty associated with the mean values is 1σ , whereas the uncertainty associated with the median values is the IQR. Vertical rate uncertainties (PL + WN noise model) from (c) unfiltered and (d) filtered time series as a function of measurement period.

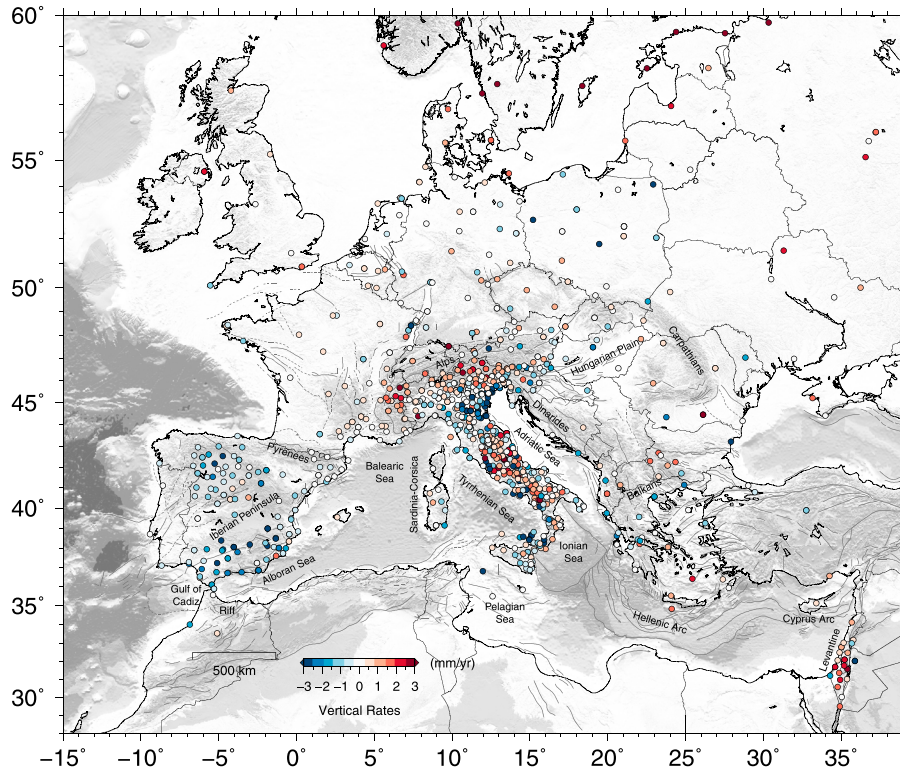


Figure 7. Map of the vertical velocity field over the Euro-Mediterranean region. The color scale is saturated at ± 3 mm/yr. Positive (red) and negative (blue) values show uplift and subsidence, respectively.

estimates because short span velocity estimate is easy to be biased by systematic errors. For the vertical velocities, we find that differences in the velocities estimated from unfiltered and filtered time series are negligible for stations with 6 years of observations, whereas this time interval reduces to >3.5 years for the horizontal velocities. For longer time span, regional filtering only impacts the uncertainties of the velocity estimates.

3.2. Noise Analysis

[25] Previous work [e.g., Langbein and Johnson, 1997; Mao et al., 1999; Williams et al., 2004] demonstrated the presence of significant time-correlated noise in the GPS position time series. An important consequence is that formal errors on the GPS-derived velocities are largely underestimated (by factors of 5 to 10) if correlations are not properly accounted for [e.g., Mao et al., 1999]. Several studies concluded that a combination of power law (PL) plus white noise (WN) models turns out to provide the most likely stochastic description of GPS position time series [e.g., Mao et al., 1999; Williams et al., 2004; Wöppelmann et al., 2009; Santamaría-Gómez et al., 2011]. In many solutions, the noise can be best described by a combination of WN and flicker noise (FN), with a spectral index $\kappa = -1$ [Agnew, 1992]. Here we do not aim at determining site-specific noise models, which will be the objective of a future work when more detailed information about individual station environments such as monumentation will be collated.

[26] We examine the noise content in our residual time series adopting the maximum likelihood estimation (MLE) technique implemented in the CATS software [Williams, 2008]. In particular, we use a recent revision (CHEETAH)

that implements the fast algorithm described in Bos et al. [2007]. We analyze both the unfiltered and filtered residual time series, with the goal of evaluating the gain in the vertical velocity accuracies from applying regional filtering of CME, as described in the previous section. We solve for a residual trend whilst simultaneously solving for the amplitudes of the WN and PL components and either fixing k to -1 (FN) or solving for k (PL model). Not estimating offsets and seasonal signals together with the velocity leads to lower formal errors but we find that this is in general not as big an effect as the inclusion of colored noise in the analysis.

[27] Figure 4 shows the frequency distribution of the κ values estimated from the analysis of unfiltered and filtered residual position time series. For both, the mean and median values of κ for the vertical component are close to -0.7 . Nevertheless, we find that the distribution of κ values for both the horizontal and vertical components estimated from filtered time series shows a greater dispersion around the mean than those obtained from the unfiltered time series. This is illustrated by the standard deviations, or the interquartile range (IQR) of the median, which for the filtered time series are close to twice that obtained from the analysis of the unfiltered time series. In both cases, the mean κ is not actually -1 but slightly less. We conclude that the spread is sufficient to rule out the general case of FN and we adopt a PL+WN noise model in estimating the vertical motions and their uncertainties for the final analysis.

[28] To easily compare noise amplitudes between the filtered and unfiltered series, we look at the FN and WN amplitudes estimated from a FN+WN error model (Figure 5) as well as the amplitudes of the PL noise from the PL+WN model. Since the PL amplitudes are dependent on κ , they

are not easily comparable. The FN amplitudes, whilst not perhaps the correct error model, do allow a degree of comparability amongst the series. We find that while the WN amplitudes from the unfiltered and filtered time series remain mostly the same, there is a significant reduction (>35%) in the amplitude of the colored noise, both assuming the special case of $\kappa = -1$ or a PL model. This suggests that the PL noise component is spatially coherent and forms most of the CME. The WN component is potentially site specific and therefore mostly unchanged when the space-time filtering is applied. The remaining colored noise in the filtered series may be a combination of residual noise from the filtering and underlying more localized effects such as monument noise at poor sites that are of such amplitude that they are undetectable in the unfiltered series. This and the change in ratio between the colored noise and WN amplitudes (colored reduced, WN unchanged) may explain the increase in standard deviation of κ estimated from the filtered series.

[29] Figure 6 shows the frequency distribution of the estimated vertical motion rates, and associated uncertainties, from both the unfiltered and filtered time series. The mean vertical velocity is close to 0 mm/yr, and 95% of the GPS stations analyzed move vertically in the range of ± 2 mm/yr. The fastest subsidence rates (11 mm/yr) are observed in the southern Tyrrhenian Sea (Italy), whereas the fastest uplift rates (6 mm/yr) are observed in northern Europe. Velocity uncertainties are in the range of 0.1 to 2 mm/yr, with a mean velocity error of 0.39 mm/yr and a standard deviation of 0.29 mm/yr. Most (95%) of the GPS stations show a velocity uncertainty < 0.95 mm/yr. It is worth noting that the uncertainties estimated from filtered time series, adopting the same noise model, are on average $> 40\%$ smaller than ones from unfiltered time series. The estimated vertical velocities and uncertainties are reported, together with other parameters, in Table S2 of the supporting information.

4. Description of the Vertical Velocity Field

[30] As anticipated in section 1, the absolute (i.e., IGS08) vertical rates might be slightly biased, with the bias evolving with latitude, and thus uplift and subsidence are not “absolute” and might be shifted in location, making difficult the interpretation of vertical rates, particularly when rates are small. Moreover, since GPS motions are tied in the global ITRF/IGS reference frame, and this frame is not fixed to the solid earth (i.e., the coordinate origin of the ITRF is tied to the center of mass of the total Earth system, not to the center of mass of the solid Earth), this may cause an unknown baseline shift between actual vertical velocities and ground motion rates as, for example, predicted by geodynamic modeling. For this reason, in order to use the vertical rates provided in this work in modeling or for comparisons with other vertical data, velocities should be realized with respect to local relative frames.

[31] The final vertical velocity field, obtained from the analysis of the filtered time series (cleaned by outliers, offsets, and seasonal terms), assuming a PL + WN noise model, is shown in Figure 7. The fastest uplift rates in the European-Mediterranean region occur north of 54°N , a signal dominated by the ongoing postglacial rebound processes [e.g., Johansson *et al.*, 2002; Nocquet *et al.*, 2005]. Since in this region our velocity estimates agree with previous solutions,

these will not be discussed here. Over central Europe, the spatial distribution of stations is quite uniform but with low density. On average, central Europe (including central and northern France) appears rather stable, with a median vertical velocity of 0.1 ± 0.9 mm/yr. Only few stations show larger velocities but generally < 1 mm/yr, probably related to local process.

[32] The Iberian Peninsula (see Figure 9 for the toponyms) has a dense spatial distribution of data, which show a rather well-constrained pattern of regional subsidence but with varying rates. Uplift is localized in central Iberia, and in southeastern Spain, few stations show positive or stable velocities. On average, the fastest subsidence rates are close to -3 mm/yr and are located in southern Spain. Along the Mediterranean coastal region, subsidence is faster close to the Gulf of Cadiz and decreases eastward, approaching zero close to the southern Pyrenees and southern France. Some of the observed features in the western Mediterranean are new, since previous solutions [e.g., Santamaría-Gómez *et al.*, 2012], although showing some similar trend at sites along the coasts of southern Spain, are significantly sparser than our geodetic solution.

[33] In the central Mediterranean area (i.e., Italy and surroundings, see Figure 10 for the toponyms), our geodetic solution is significantly denser than in other regions and in comparison to previously published works [Baldi *et al.*, 2009; Devoti *et al.*, 2010, 2011; Bennett *et al.*, 2012] showing spatially coherent vertical velocity patterns both at short and long spatial scales. The Alpine domain shows a general uplift. Faster uplift rates (~ 2 mm/yr or even faster at few points) are observed in the western and central Alps, and decrease toward the eastern Alps to stable or negative values up to -2 mm/yr in the Slovenian Alps (east of 13°E). In the Pannonian-Carpathians region, the number of stations is more limited and the velocity field indicates a slow subsidence in the Hungarian plain and stable or slow uplift in the Carpathians.

[34] The Po Plain (northern Italy, see Figure 10 for the toponyms) is rather stable in its western sector, showing increasing subsidence rates (faster than -3 mm/yr) toward the northern Adriatic coasts, where subsidence rates are as large as -8 mm/yr (e.g., near the Po River delta), and fast subsidence rates at sites near the NW-SE striking northern Apennines frontal range. In the Apennines chain, we observe significant changes in the vertical velocity pattern both along and normal to the chain axis. While the northern Apennines (i.e., the Tuscany and Emilia-Romagna sectors) show slow vertical velocities and a general slow subsidence, the central (~ 2 mm/yr) and southern (~ 1 mm/yr) sectors of the Apennines chain clearly show uplift. This positive signal is localized along the chain axis, characterized by the higher topographic relief, particularly in the southern Apennines (i.e., Campania and Basilicata).

[35] In Calabria (southern Italy), we find difference between its western subsiding (Tyrrhenian) side, with rates close to -3.5 mm/yr, and its eastern uplifting (Ionian) side, with rates close to 1.5 mm/yr. A fast subsidence characterizes the central Aeolian Islands (southern Tyrrhenian Sea), where we find the fastest subsidence rates of the central Mediterranean region (down to ~ -10 mm/yr). Vertical velocities in Sicily show slow subsidence in the southeast (< -1 mm/yr), which turn into slow uplift rates (< 1 mm/yr) in the north, along the

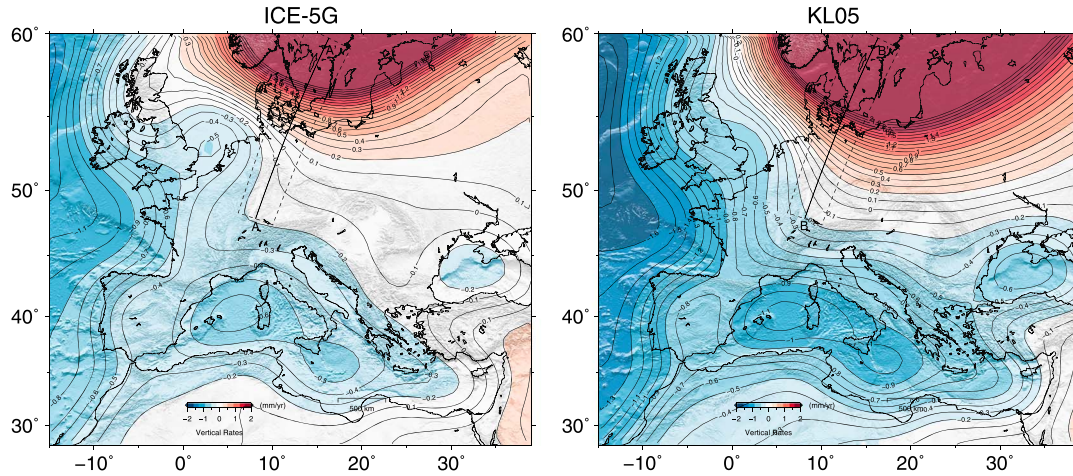


Figure 8. Predicted vertical surface motion rates due to glacial isostatic adjustment (GIA) in the Euro-Mediterranean area obtained adopting our implementation of the ICE-5G and the KL05 models, respectively. The A-A' and B-B' lines and the dashed boxes refer to the cross sections plotted in Figure S6.

Nebrodi and Madonie Mountains. To the south, the Pelagian stations Malta and Lampedusa are stable, while the Pantelleria volcanic island is subsiding at fast rates (~ -3 mm/yr).

[36] On the eastern side of the Adriatic Sea, the number of GPS stations available in our solution is limited, and the few vertical velocities are close to zero (northern and central Croatia) or negative (~ -1 mm/yr) in southern Croatia. In Albania, the few sites available show variable vertical velocities, including uplift and subsidence, and do not provide significant indications. On the contrary, in the Balkans Mountains of Bulgaria, we find a rather coherent uplift at rates of ~ 1.5 mm/yr. The limited number of stations in the Hellenic arc indicates a coherent pattern with continental Greece and Corinth Gulf subsiding down to ~ -2 mm/yr and Crete and the Cyclades uplifting at rates of ~ 1.0 mm/yr.

[37] In the eastern Mediterranean, aside two station at Cyprus and in southern Turkey, a coherent and robust solution in the Levantine (mainly in Israel) highlights an increasing rate of uplift, up to ~ 2 mm/yr, closer to the Dead Sea fault trace.

5. Postglacial Rebound Component of Vertical Velocities

[38] The measured velocities result from the combination of geodynamics, tectonics, GIA, and other unknown processes. Accounting for GIA is fundamental for the interpretation of sea level and modeling of geodynamic processes [e.g., Lambeck and Purcell, 2005; Stocchi et al., 2005]. Here the effect of GIA at GPS sites is modeled by an improved version of the open-source code SELEN [Spada and Stocchi, 2007]. SELEN numerically solves the sea level equation [Farrell and Clark, 1976], which describes the spatiotemporal variations of sea level associated with melting of the late Pleistocene ice sheets, for a laterally homogeneous, spherical, and self-gravitating Earth with Maxwell rheology, including the effects of rotational fluctuations on sea level [Milne and Mitrovica, 1998] and accounting for horizontal migration of shorelines [Peltier, 2004].

[39] In our GIA computations, we have implemented two global models characterized by distinct mantle rheologies and time histories of the mass of continental ice sheets since the Last Glacial Maximum (LGM). The two models are constrained by different global data sets of relative sea level variations since the LGM, which motivates their different parameterizations. These are the ICE-5G (VM2) [Peltier, 2004] (hereafter indicated as ICE-5G) and the ice model progressively developed at the Research School of Earth Sciences of the National Australian University [Lambeck et al., 1998, and subsequent contributions]. Since this latter ice model is valid as of 2005, it is referred to as KL05 in the following. The ICE-5G model does not account for the melting of the Alpine ice cap, while the KL05 models does. This contribution has been evaluated by Stocchi et al. [2005], finding that it accounts for a small fraction ($\sim 10\%$ in the western Alps) of the estimated vertical GPS rates.

[40] The viscosity profiles of ICE-5G and KL05 mainly differ in the lower mantle, where the adopted average viscosity values are 2.7 and 2.0×10^{21} Pa s, respectively. As discussed by Stocchi and Spada [2009], lower mantle viscosity has a major role in the assessment of present-day sea level variations and vertical movements associated with GIA across the Mediterranean Sea. Models characterized by a relatively large lower mantle viscosity have the tendency to produce faster displacement rates at present, because of the larger isostatic disequilibrium implied. Other model parameters such as the shallow upper mantle viscosity (0.5 and 0.3×10^{21} Pa s in ICE-5G and KL05, respectively) and the thickness of the elastic lithosphere (90 and 65 km) play a comparatively minor role. As noted by Stocchi et al. [2009], the GIA-induced sea level variations in the Mediterranean are particularly sensitive to the melting chronology of the Antarctic ice sheet, which differ significantly in the two GIA models (a short account of these differences has been recently given by Spada and Galassi [2012]).

[41] Our GIA predictions are given in the reference frame of the center of mass of the whole Earth, so it is nominally comparable with our absolute IGS08 estimates. Figure 8 shows the GIA velocities over the Euro-Mediterranean region predicted adopting the two models described above

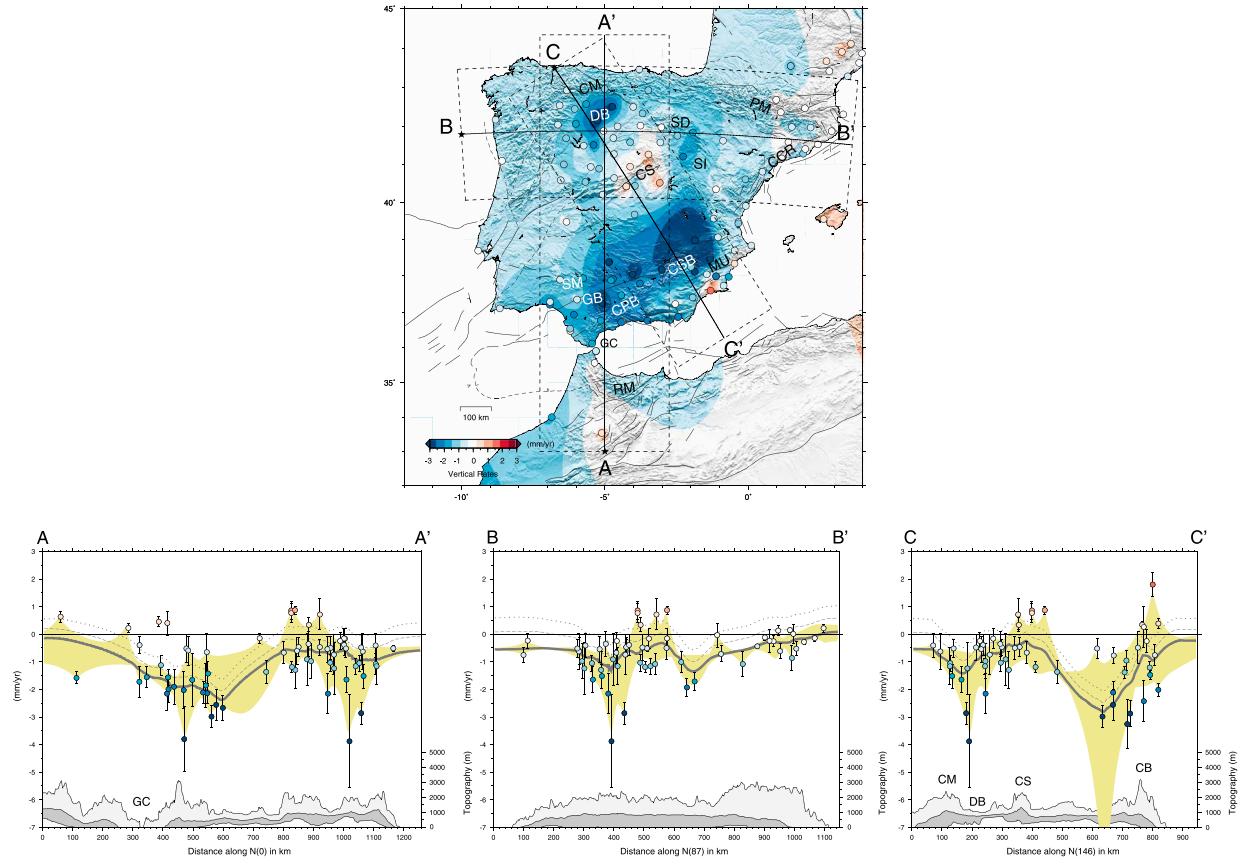


Figure 9. (top) The observed vertical velocity field (colored circles) with color contour representing a smoothed spline model fit to the estimated rates over the Iberian region (see main text). The color scale is saturated at ± 3 mm/yr. Positive (red) and negative (blue) values represent uplift and subsidence, respectively. The dashed lines show the position of the swath profiles plotted in Figure 9 (bottom). GC: Gulf of Cadiz, RM: Riff Mountains, PM: Pyrenees Mountains, DB: Duero Basin, CCR: Catalan Coastal Range, MU: Murcia, CPB: Cordillera Para Betica, CSB: Cordillera Sub Betica, GB: Guadalquivir Basin, SM: Sierra Morena, CS: Central System, SD: Sierra de la Demanda, SI: Sistema Iberico. (bottom) Three cross sections of the observed vertical velocities (colored circles), with 1σ uncertainty error bars, of GPS stations included in the dashed boxes (A-A', B-B', and C-C'). The symbols are plotted adopting the same color scale as in the map. The grey line shows the median value estimated from the smoothed spline fit of the vertical velocity field, while the yellow envelope shows the minimum and maximum vertical rates values in the swath, filtered using a robust 10 km Gaussian filter. The swath topographic profile is also plotted, with the dark grey profile showing the average (median) topography in the swath, while the light grey and white profiles showing the maximum and minimum elevations, respectively. The topographic profiles are filtered using a 10 km Gaussian filter. The dotted and dashed lines show the median value estimated from the smoothed spline fit of the vertical velocity field corrected for the GIA component using the KL05 and ICE-5G models, respectively.

(Table S2 shows the specific values at the GPS sites). The pattern of GIA surface velocities is similar for the two models. Northern Europe displays a dome-shaped uplift pattern, which reflects the well-known flexural response to ice unloading. Around the Mediterranean, both models predict a broad pattern of subsidence, which mostly reflects the response to the meltwater loading that deforms the seafloor. Rates of subsidence increase toward the bulk of the Mediterranean Sea, where faster rates are predicted for the Balearic and Ionian Sea, and toward the Atlantic Ocean. GIA velocities predicted by the two models show some remarkable differences. In particular, velocities obtained using the KL05 model show a steeper gradient in central Europe

and faster subsidence rates in the bulk of the Mediterranean and in western Europe. Figure S6 in the supporting information shows two cross sections, oriented about normal to the steeper gradients predicted by the two models, located on nontectonically deforming regions of Europe, where GPS velocities and GIA predictions are compared. While KL05 seems to fit better uplift rates in northern Europe than ICE-5G, in central Europe, GPS sites are stable or slowly subsiding, and GIA models would predict very slow subsidence rates. Differently from *Nocquet et al.* [2005], our GIA predictions do not show a marked zone of subsidence surrounding the uplift area, and this is due to the use of different ice and Earth models. It is out of the scope of this work to comment

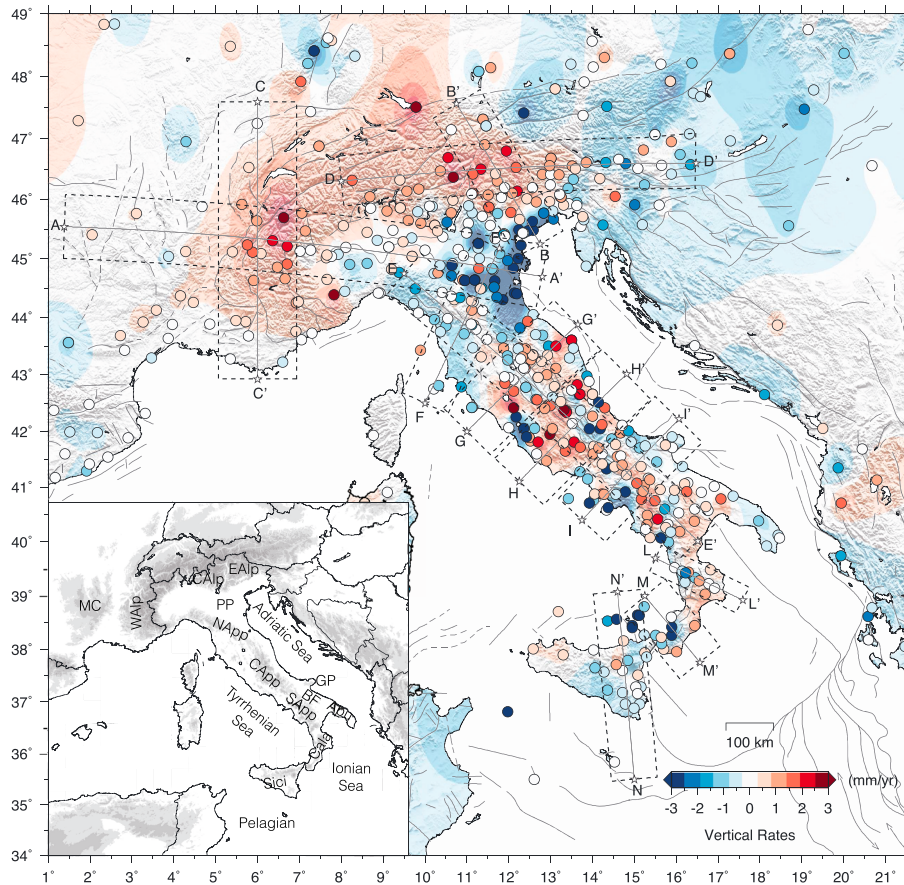


Figure 10. Observed vertical velocity field (colored circles) and color contour representing a smoothed spline model fit (see main text) to the estimated rates over the Italian and surrounding regions. The color scale is saturated at ± 3 mm/yr. Positive (red) and negative (blue) values represent uplift and subsidence vertical velocities, respectively. The dashed lines show the position of the swath profiles of Figures 11–13. The bottom left inset shows some geographical areas mentioned in the text. MC: Massif Central, WAIP: Western Alps, CAIP: Central Alps, EAIP: Eastern Alps, PP: Po Plain, NApp: Northern Apennines, CApp: Central Apennines, SApp: Southern Apennines, BF: Bradanic Foredeep, GP: Gargano Promontory; Apu: Apulian platform; Cala: Calabrian Arc, Sici: Sicily.

in details the reasons for such differences, but we believe that using two independently derived GIA models provides, for our purposes, a rough estimate of the uncertainty associated with GIA modeling across the Euro-Mediterranean region. Applying the GIA correction to the measured vertical velocities at GPS sites around the Mediterranean changes the GPS rates by up to 0.5 to 1 mm/yr, depending on the model used, which, in general, gives faster uplift rates and slower subsidence rates, as shown in the cross sections presented in section 6.

6. Vertical Velocity Gradients, Topography, and Geodynamic Implications

[42] We plot vertical velocities along cross sections sampling different sectors of the Euro-Mediterranean region, particularly those where a denser distribution of GPS stations is available in our geodetic solution. We interpolate the observed discrete vertical velocities using an adjustable tension continuous curvature surface gridding algorithm [Smith and Wessel, 1990]. The interpolated vertical velocity fields for the western, central, and eastern Mediterranean, together

with traces of the cross sections, are shown in Figures 9, 10, and 14, respectively. Velocities (with 1σ error bars) of GPS stations located inside the profile swath are plotted with respect to the distance along the profile track, together with the median, maximum, and minimum values of the vertical rates, estimated from the smoothed velocity field and sampled at steps of 1 km along the swath profile. The cross sections highlight some remarkably new features of the ground motion rates measured by GPS, which are discussed in the next sections.

6.1. Iberia

[43] The morphological structure of the Iberian Peninsula is characterized by a moderate average elevation, together with flat surface (the so-called Iberian Meseta). Much of this topography feature has been acquired recently post-Miocene/Pliocene age, postdating the main compressional phases [e.g., Casas-Sainz and de Vicente, 2009]. Tectonic activity is mainly confined in southern Iberia and the Pyrenees, where significant geodetic strain rates have also been measured [Stich et al., 2006; Serpelloni et al., 2007], whereas central and northern Iberia appear tectonically stable.

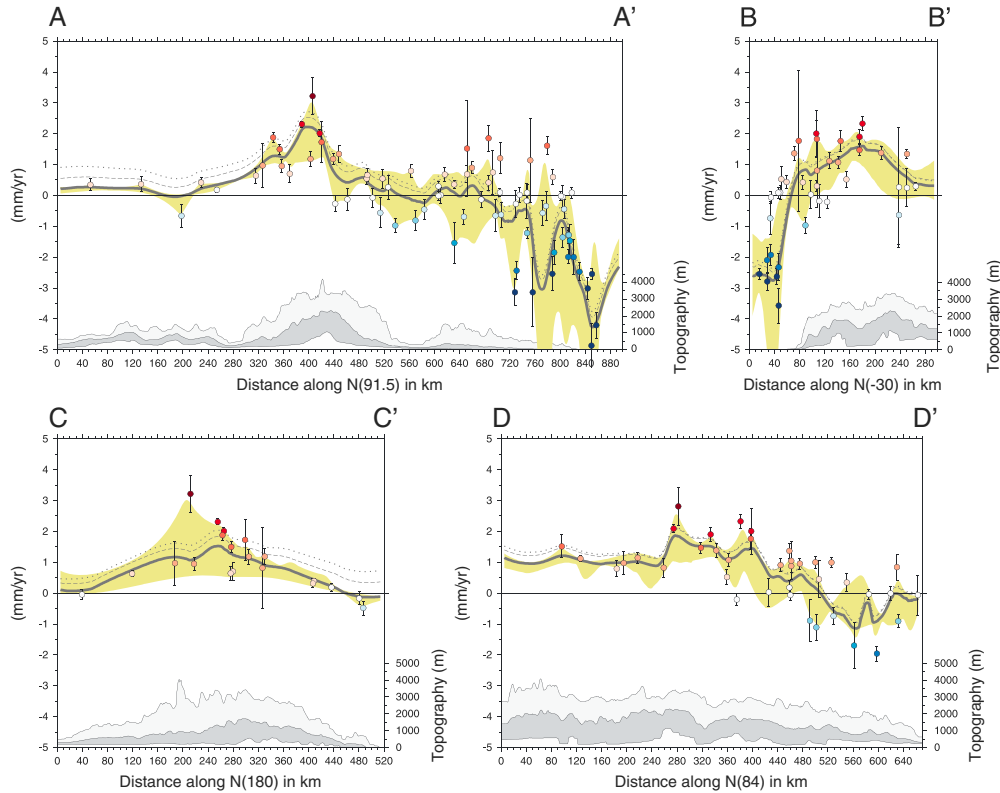


Figure 11. Cross sections of the observed vertical velocities in the Alpine region. Letters refer to the profiles in Figure 10. Velocities and topography are plotted following the conventions of Figure 9.

[44] The cross sections in Figure 9 highlight undulations of the vertical velocity patterns both N-S (A-A') and E-W (B-B'), occurring at both long spatial lengths (>300 km), as along the A-A' profile, and shorter spatial lengths (~ 100 km) as along the B-B' profile. The A-A' profile shows a steep velocity gradient (~ 2.5 mm/yr in few tens of km) with ground motions changing from slow uplift at the few Moroccan sites to subsidence (down to -2 mm/yr) along southwestern Spain's coasts. Crossing the Cordillera Bética, the Guadalquivir Basin, and the Sierra Morena, subsidence rates increase to -3 mm/yr, decreasing to ~ -1 mm/yr moving northward (after km 800 of the profile). Here we find faster subsidence rates (down to -3 mm/yr) in the Duero Basin and uplift (up to 1 mm/yr) at few stations located near the Central System mountain range. The B-B' profile in northern Iberia highlights a transition from slow subsidence in Portugal (< -1 mm/yr) to mostly null ground motions in the eastern sector of the Pyrenees Mountains-Catalan Coastal Range, where the velocity gradient roughly follows the shape of maximum elevations. In between, we find undulations of the velocity pattern, with uplifting stations near the Central System and increasing rates of subsidence (down to ~ -2 mm/yr) at the few sites located around the Sierra de la Demanda e Sistema Ibérico.

[45] The C-C' profile is most illustrative as it runs normal to the main tectonic structures in Iberia and better illustrates the long wavelength undulations of the vertical velocity field. Rates of subsidence increase moving from the Cantabrian Mountains to the Duero Basin, from ~ -1.5 mm/yr to ~ -3 mm/yr. Then, subsidence rates smoothly decrease southeastward and crossing the uplifting Central

System (~ 1 mm/yr). Moving southeastward, fast negative vertical rates are present in Murcia (down to -3 mm/yr). Between km 640 and 760 of the profile, we find a steep velocity gradient (>2 mm/yr in ~ 120 km) with a rapid decrease of subsidence rates and a transition to stable ground motion, up to slow uplift (below 0.5 mm/yr) localized across the Cordillera Bética.

[46] The calculated GIA component in the study area is a smooth long wavelength pattern, and thus correcting the measured GPS velocities for the GIA contribute over Iberia does not significantly change the observed gradients. The most important effect is a reduction in the rates of subsidence in the range of 0.5–1 mm/yr, depending on the global model adopted in the GIA computations (see section 5).

[47] The interpretation of the vertical velocity field and its linkage with the morphology of Iberia is not as simple. Possible models suggest that the origin of Iberian topography and undulations could be related to lithospheric folding, causing the differential uplift of different parts of the Iberian plate and controlling the distribution of basins and mountains chains, bounded by folds and faults [Cloetingh *et al.*, 2002; De Vicente *et al.*, 2007]. Another possible hypothesis proposes that topography could be linked to mantle dynamics [Fernández *et al.*, 1998]. Residual topography calculated using global (Crust 2.0) [Bassin *et al.*, 2000] and regional [Tesauro *et al.*, 2008] models show that topography is in fact not compensated by crustal isostasy. Dynamic topography models show a positive signal over the north and central Iberia [Faccenna and Becker, 2010] related to the presence of shallow low velocity anomaly located in the uppermost mantle [Boschi *et al.*, 2010].

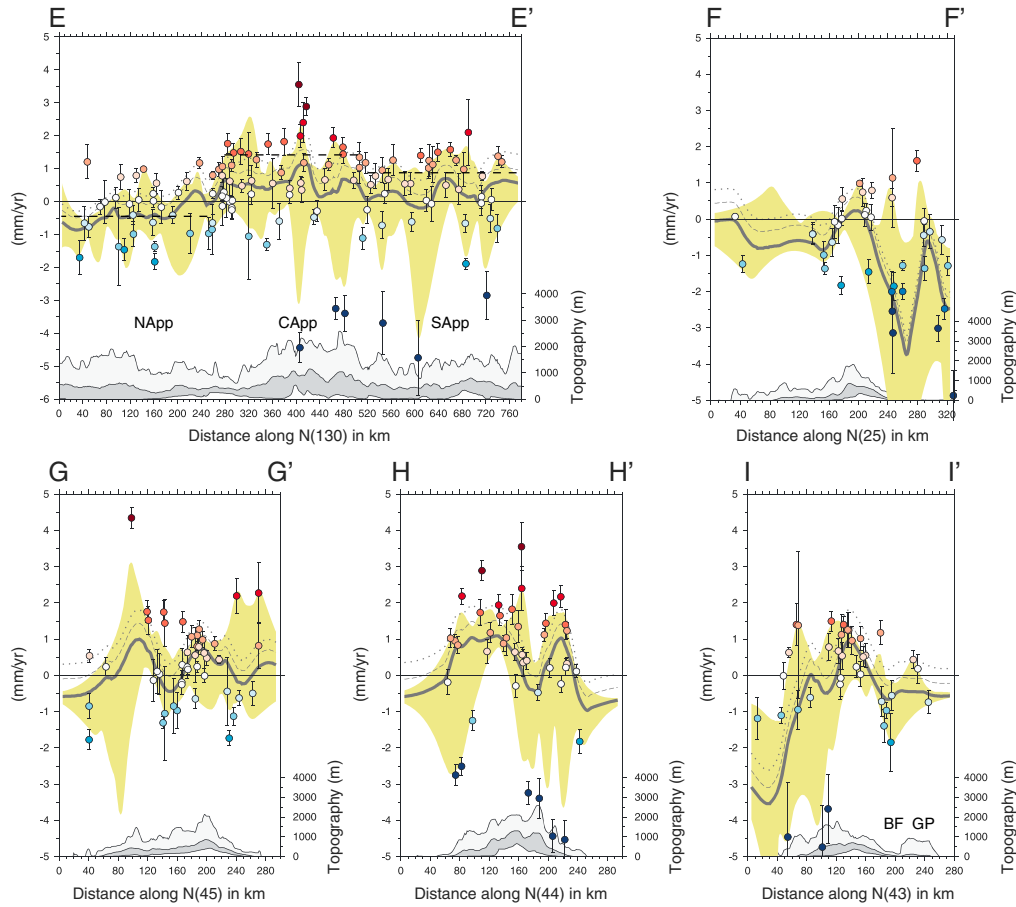


Figure 12. Cross sections of the observed vertical velocities in the Apennines region. Letters refer to the profiles in Figure 10. Velocities and topography are plotted following the conventions of Figure 9. NApp: Northern Apennines, CApp: Central Apennines, SApp: Southern Apennines, BF: Bradanic Foredeep, GP: Gargano Promontory.

[48] Our GPS solution for Iberia shows a distributed pattern of subsidence with a relatively poor fit between vertical motion and topographic signatures. Two well-marked subsiding regions bound the north and south (Guadalquivir Basin/Cordillera Sub Betica) of the uplifting Central System (see C-C' profile). If this signal is confirmed, we are left to imagine that the actual vertical motion is a relatively recent feature not yet registered in the topography trend, with the exception of the Central System. Further studies are needed to be able to understand the cause of the observed vertical motions. The lithospheric folding model [Cloetingh *et al.*, 2002; De Vicente *et al.*, 2007] could explain the basin and swell structure, according to patterns observed in the C-C' profile. Mantle dynamic models could also be involved assuming that the anomaly that produced the general uplift of Iberia is now cooling down at the base of the lithosphere inducing subsidence. Convection models are needed to understand the role of mantle dynamics on the topography and surface velocity of Iberia.

6.2. The Alps

[49] The Alps represent the largest elevated mountain belt in the Mediterranean. Horizontal deformation is dominated by the counterclockwise rotation of the Adria microplate around an Euler pole positioned at the boundary between

the Po Plain and the western Alps foothills [Battaglia *et al.*, 2004; Nocquet and Calais, 2004; D'Agostino *et al.*, 2005], causing compression in the eastern Alps, dextral shear in the central Alps, and transtension or very slow deformation in the western Alps. The estimated geodetic vertical velocity field shows a rather continuous positive vertical signal along the Alpine mountain range, with rates ranging between ~ 1 and ~ 2 mm/yr, with maximum values concentrated in the western French Alps and the eastern Italian Alps (see Figures 11 and 12). Although our velocity solution misses GPS sites in the Swiss Alps, precise leveling data [Schlatter *et al.*, 2004] provide clues on maximum uplift rates of ~ 1.3 mm/yr positioned just east of the Lake of Costanza, on the core of the Alpine belt, suggesting a spatial continuity with our data in the western French Alps.

[50] The A-A' and C-C' profiles of Figure 11 highlight a correlation between vertical velocities and topography in the western Alps. In particular, A-A' shows, from W to E, a rapid transition from small uplift (~ 0.5 mm/yr) in the Massif Central (France) to fast uplift rates (up to 2 mm/yr) in correspondence of the highest topographic relief of the western Alps, with a gradient > 3 mm/yr over ~ 150 km. Eastward, uplift rates rapidly decrease and velocities turn to subsidence (at rates of ~ 1 mm/yr), at the junction between the western Alps and the northern Apennines of Italy.

[51] The B-B' profile in Figure 11 crosscuts the eastern Alps. It shows a steep velocity gradient of ~ 3.5 mm/yr in ~ 80 km, from the subsiding northern Adriatic area (with rates down to -2.5 mm/yr) to fast uplift rates (~ 2 mm/yr) in the internal Alpine domain (i.e., Dolomites and South Tyrol), following the steep topographic gradient.

[52] The E-W trending D-D' profile of Figure 11 outlines a steep gradient (~ 1 mm/yr over few kilometers) in the central Alps, where uplift rates reach values >2 mm/yr. Moving eastward, it shows a smooth decrease of the uplift rates toward a prevailing subsidence in the Slovenian Alps. This smooth velocity gradient follows the decreasing elevations of the chain.

[53] All alpine cross sections in Figure 11 show a correlation between vertical velocities and topography in the Alps. GIA correction could only slightly modulate the values (by a positive amount that is larger in the western Alps than the eastern Alps) but not the trend. Three different hypotheses can be put forward to explain the uplift of the Alps: (i) erosion-driven isostatic topography, (ii) tectonic-driven isostatic topography, and (iii) mantle supported (dynamic) topography.

[54] (i) Erosion processes lower the mean elevation but favor uplift of mountain peaks [Molnar and England, 1990]. The expected linear relationships between ^{10}Be cosmogenic denudation rate and geodetic uplift rates in the central Alps have been taken as a prove that part of the uplift in the Alps is related to erosion unloading [Wittmann et al., 2007; Champagnac et al., 2009]. Elastic isostatic calculations provide rates of uplift of about 0.5 to 0.8 mm/yr [Champagnac et al., 2007, 2009].

[55] (ii) Crustal thickness in the western Alps deepens from 30–35 km to reach ~ 50 –55 km in the more internal units [Lombardi et al., 2008]. In the central Alps, where structure is better illuminated by CROP experiments, crustal thickness also reaches ~ 55 km depth in the internal zone. The motion of the Adria plate, and its collision with the Alpine range [D'Agostino et al., 2005; Bennett et al., 2012], can only partly explain the compressional and uplift field related to active thrusting observed in the eastern-southern Alps. However, it cannot provide an explanation for the uplift of the western or central Alps where there are no signs of active compressional deformation.

[56] (iii) The deep structure of the Alps, as defined by seismic tomography, is characterized by a high-velocity body plunging down to 200–300 km in the western and central Alps [Lippitsch et al., 2003; Piromallo and Faccenna, 2004], whereas in the eastern Alps, the structure is less clear, a subvertical body does not look directly connected to the surface, while high-resolution models here reveal a steep slab-like body, or slightly northward plunging body, in the depth range 150–300 km [Lippitsch et al., 2003]. The deeper portion of the Alpine slab is detached from the shallower portion most probably around ~ 30 –35 Ma [von Blanckenburg and Davies, 1995]. Those deep mantle processes can indeed contribute with surface process to the vertical motion; however, the exact response and how mantle forces surface motion are still poorly understood.

[57] The correlation between vertical velocity, elevation, and erosion suggests that topography in the Alps results from continuous ongoing uplift and erosion processes. A large fraction of that uplift can be reasonably related to erosion

unloading, and in the eastern Alps a fraction can be also related to active shortening.

6.3. Po Plain

[58] Section A-A' in Figure 11 shows increasing rates of subsidence moving from west to east along the Po Plain longitudinal axis, with a steep gradient near the Adriatic coasts, where rates rapidly reach values faster than -4 mm/yr. Section F-F' in Figure 12 shows a steep gradient across the northern Apennines front, with a rapid transition from slow uplift to fast (> -3 mm/yr), northeastward, decreasing subsidence. Correction of the observed velocities for GIA reduces the rates of subsidence in the Po Plain but does not affect the observed gradients.

[59] According to Bennett et al. [2012], a larger part of the geodetic rates is probably related to long-term subsidence, since it appears to be independent of cities (with anthropogenic effects, such as groundwater pumping) and is observed over distances in excess of 100 km. Long-term subsidence could be caused by loading associated with rapid sedimentation [Bertotti et al., 1997; Picotti and Pazzaglia, 2008; Carminati et al., 2003a], or could represent a flexural response to slab sinking [Carminati et al., 2003b]. In addition, the NE decrease of the subsidence rates (F-F' profile in Figure 12) could be associated with tectonic activity of the northern Apennines external thrust front, buried beneath the Po Plain sediments, which also recently ruptured during the 2012 Emilia earthquake sequence [Serpelloni et al., 2012b; Pezzo et al., 2013]. The great spatial variability of subsidence rates in the Po Plain depends on various natural and anthropogenic processes [Carminati and Martinelli, 2002], including compaction of alluvial deposits of different thickness and compaction of sediments undergoing stress state variations due to intense fluid withdrawal from shallow aquifer systems or gas reservoirs [e.g., Brighenti et al., 1998; Bitelli et al., 2000; Teatini et al., 2006; Giambastiani et al., 2007].

6.4. The Apennines

[60] Although rather scattered, the E-E' profile in Figure 12 highlights a change in the median of the smoothed vertical velocity field, with maximum rates of uplift in the central Apennines (up to 2 mm/yr in the Abruzzi Apennines) decreasing toward the northern Apennines that are characterized by subsidence (down to -1.5 mm/yr) or rather stable ground motions, and southward in the southern Apennines, where uplift rates are on average ~ 1 mm/yr. Correcting the measured GPS velocities for GIA decreases the subsidence rates and increases uplift rates by amounts that are increasingly larger from north to south, using both the ICE-5G and KL5 models. In particular, in the southern Apennines, the GIA contribution is as high as 1 mm/yr, according to the KL05 model.

[61] The F-F' profile in Figure 12 cross cuts the northern Apennines and Po Plain, showing a transition from subsidence (at ~ -1 mm/yr) to uplift with a steep gradient of ~ 2 mm/yr in ~ 50 km across the extensional Tuscany basins and the chain axis. Maximum uplift rates (of ~ 1 mm/yr) coincide with the highest topographic elevations, in agreement with leveling measurements [D'Anastasio et al., 2006]. Moving northeastward, a steep gradient of >3 mm/yr over ~ 30 km characterizes the transition from the mountain front to the southwestern Po Plain, discussed in section 6.3. Correcting the GPS velocities for GIA results in decreasing

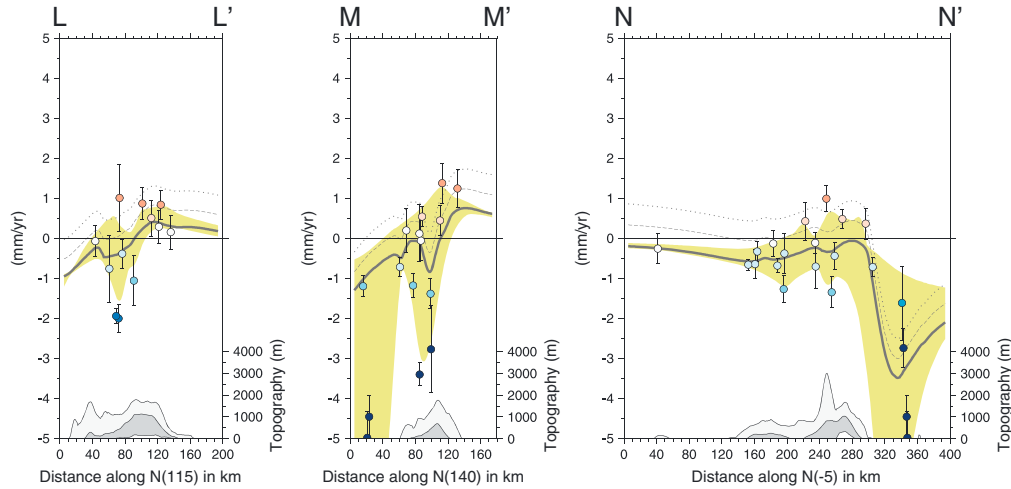


Figure 13. Cross sections of the observed vertical velocities in Calabria and Sicily. Letters refer to the profiles in Figure 10. Velocities and topography are plotted following the conventions of Figure 9.

rates of subsidence in Tuscany and increasing rates of uplift at the front of the northern Apennines. Using the KL05 model results in a median rate that is 1 mm/yr faster.

[62] The G-G' and H-H' profiles in Figure 12 crosscut the Umbria-Marche and Lazio-Abruzzi sectors of the central Apennines and the I-I' profile runs across the southern Apennines and Gargano promontory. They all show an overall correlation between topography and the median of the interpolated vertical velocities over the length scale of the mountain range (~200 km), with a transition from subsidence in the Tyrrhenian side to uplift in the inner side of the chain, decreasing on average toward the Adriatic. The G-G' and H-H' profiles highlight undulations of the vertical velocity pattern occurring at a shorter length scale (<100 km), with steep velocity gradients about in correspondence of the highest topographic peaks and extensional faults of the intermountain basins. A similar pattern has also been observed from the analysis of precise leveling data [D'Anastasio *et al.*, 2006]. The I-I' profile shows a steep gradient toward the Bradanic foredeep (~3 mm/yr in 40 km) and a less constrained slow uplift at the few sites in the Gargano promontory.

[63] As for the Alps, in the Apennines, we find a correlation between vertical rates and topography, with faster uplift at the mountain peaks, and it is possible to distinguish between three different mechanisms to explain this velocity pattern: (i) erosion-driven isostatic topography, (ii) tectonic-driven isostatic topography, and (iii) mantle-supported (dynamic) topography.

[64] (i) Erosion represents a possible driving factor to lower the elevation of a belt. For the case of the Apennines, erosion could not only have been caused by transport of mass away from high elevation by rivers [Westaway and Bridgland, 2007] and local small glaciers but also caused by normal faulting [e.g., D'Agostino *et al.*, 2001]. Most probably, the presence of a less erodible carbonate platform in the central Apennines could have preserved relief with respect to the silicoclastic sequences outcropping in the northern Apennines. But, as for the Alps, erosional unloading could be responsible for only a small fraction of the uplift rate.

[65] (ii) The Apennines relief formed during the last million of years, prior to that, most of the area was under marine

sedimentation. The buildup of the Apennines is related to tectonic processes and has been produced by crustal thickening due to thrusting. Thrusting along the central and southern Apennines and along the southern part of the northern Apennines vanished during the last 500 kyr. The present-day Moho depth beneath the Apennines, from receiver function, shows >50 km of crust in the northern Apennines, decreasing to ~40 km in the central Apennines [Piana Agostinetti and Amato, 2009]. Therefore, we should expect the northern Apennines to be more elevated than the central ones. This is not the case as the central Apennines average elevation is twice (~600–800 m above sea level (asl)) that of the northern Apennines (~200–400 m asl). This indicates that crustal thickening may have contributed only partly to present-day elevations. In addition, uplift is concentrated along the axis of the belt, whereas shortening and hence uplift is expected on the frontal thrust. Frontal thrusting may be active, as for the case of the northern Apennines [Picotti and Pazzaglia, 2008], but modern maximum shortening velocities along the northern central Apennines, as measured by GPS, are of ~1–2 mm/yr [Bennett *et al.*, 2012], so the vertical component along a shallow dipping thrust is at best reduced to a small fraction of that. In addition, the location of the maximum vertical velocity along the regional divide can hardly be related to the activity of frontal thrusting that likely causes uplift of the more external (i.e., Adriatic side) portion of the chain. Maximum uplift in the Apennines is located on the divide where chain-normal extension is active, as observed by earthquake focal mechanisms, geology, and geodetic data [Hunstad *et al.*, 2003; Serpelloni *et al.*, 2005]. The interactions between the regional uplift and active normal faulting are clearly expressed in the evolution of the drainage network and the Quaternary sedimentation in the intermountain basins [D'Agostino *et al.*, 2001].

[66] (iii) Subduction and/or delamination is still ongoing beneath the northern Apennines, the region where positive vertical velocity is less relevant. Beneath the central and southern Apennines, conversely, a low-velocity anomaly is located at shallow mantle depth, down to ~200–100 km, as revealed both by *P* wave teleseismic and regional data set [Wortel and Spakman, 2000; Piromallo and Morelli, 2003;

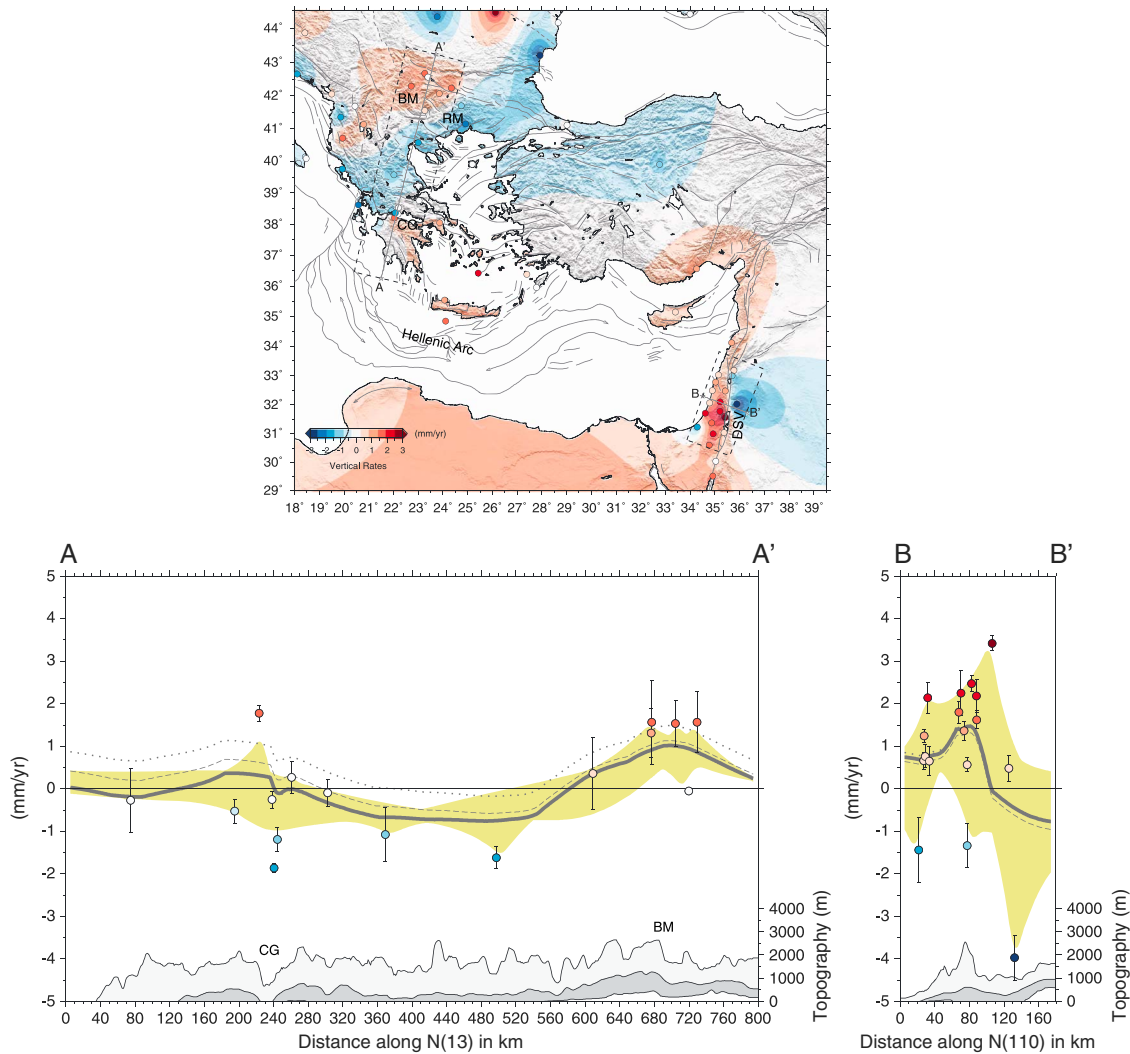


Figure 14. (top) The observed vertical velocities (colored circles) and color contour representing a smoothed spline model fit (see main text) to the estimated rates in Greece and Levantine regions. (bottom) The cross sections of the observed vertical velocities along the A-A' and B-B' profiles. Velocities and topography are plotted following the convention of Figure 9. CG: Corinth Gulf, BM: Balkan Mountains; RM: Rhodope Mountains; DSV: Dead Sea Valley.

Giacomuzzi *et al.*, 2011] and high attenuation [Mele *et al.*, 1997]. This has been commonly related to slab breakoff [Wortel and Spakman, 2000]. Active subduction is expected to depressed elevation because of the pull of the subducting slab [Mitrovica *et al.*, 1989; Gurnis, 1992; Husson *et al.*, 2012], but very few estimates are available for real Earth [Dávila *et al.*, 2010; Husson, 2006; Husson *et al.*, 2012]. On the other side, slab breakoff is expected to produce uplift of the overriding plate because of the release in downgoing suction and elastic rebound effect to flexure of the downgoing plate [Buiter *et al.*, 2002]. But the timescale and velocity of this process are disputed and could be masked or delayed by the dynamic effect related to viscous drag exerted by the falling detached portion of the slab [Gerya *et al.*, 2004].

[67] Our analysis reveals that vertical GPS velocities over the Apennines predominantly reflect the topography, suggesting that the present-day velocity was probably active

over a longer timescale and it is responsible for the Apennines topography. The uplift of the central southern Apennines is on the order of ~ 1 mm/yr (larger if GIA is included). While a fraction of this velocity may be due to erosional unloading, the remaining larger part has to be related to mantle processes.

6.5. Calabria and Sicily

[68] Figure 13 shows profiles through the Calabrian Arc (L-L' and M-M') and the Nebrodi-Peloritani Mountains in eastern Sicily (N-N'). Both L-L' and M-M' cross sections show a similar asymmetric pattern in vertical ground motion rates, with a Tyrrhenian side characterized by subsidence, which is faster in the central Aeolian, and an Ionian side showing uplift at rates of ~ 1 mm/yr, correlated with the highest topography of the Sila massif and Aspromonte. The N-N' profile shows a smooth transition from a rather stable Pelagian domain, as confirmed by the stable Lampedusa

and Malta islands (see Figure 10), to slow subsidence in southeastern Sicily (at ~ -0.5 mm/yr). In northern Sicily, a few sites show slow uplift (at ~ 0.5 mm/yr) that rapidly changes to subsidence in the central Aeolian Islands, where we find the fastest subsidence rates of the study region, down to rates faster than ~ -5 mm/yr. In Sicily and Calabria, the GIA correction is larger than that in other regions, and up to 1 mm/yr if the KL05 model is adopted. However, beyond the rate changes, velocity gradients remain unchanged.

[69] Geodetic rates in Calabria are well correlated with the geological ones. Calabria, in fact, is characterized by spectacular marine terraces and associated deposits, and many studies have been carried out to define the ages of the Calabrian terraces and to derive the related uplift rates [Antonoli *et al.*, 2006]. The oldest marine terrace detected on top of Aspromonte and Le Serre and is assigned to the early Pleistocene time, providing an average uplift rate of ~ 1 mm/yr [Miyauchi *et al.*, 1994]. The Marine Isotopic Substage (MIS) 5.5 terraces, age between 132 and 116 ka, commonly referred to as the Tyrrhenian/Eutyrrhenian stage, are well mapped and constrained [Ferranti *et al.*, 2006]. On average, the altitude of the terrace is around 100 m asl, with the largest elevations in the Messina Straits area and in the northern side of the Sila and southern Pollino massifs and the lower elevation in Le Serre range. Average uplift rates are therefore around 0.8 mm/yr [Ferranti *et al.*, 2006] while Olocene uplift rate from tidal notches is slightly higher, at around 1–1.2 mm/yr [Antonoli *et al.*, 2006], in good agreement with the geodetic rates. In addition, the altitude of the marine terraces on the Tyrrhenian side is lower than that on the Ionian side, with the notable exception of the Capo Vaticano promontory [Ferranti *et al.*, 2006], in agreement with the geodetic observations.

[70] The tectonic interpretation of uplift in Calabria is still debated. Overall, it is correlated with that observed along the Apennines belt. The difference here is that Calabria is sitting on top of an active Wadati-Benioff zone, related to the subduction of the narrow Ionian Ocean. Overall, the region is uplifting less than the central southern Apennines. This decrease may be due to the pull of the active downgoing slab [Faccenna *et al.*, 2011]. Part of the uplift could be due to elastic strain buildup at the subduction interface in the Ionian Sea, although uncertainties in the shallow geometry of the subduction interface and in the kinematic boundary condition of the Ionian-Calabria convergence make difficult to evaluate this component [Serpelloni *et al.*, 2010].

6.6. Eastern Mediterranean (Greece, Balkans, and Levantine)

[71] Despite the limited number of GPS stations in the eastern Mediterranean region, some remarkable features show up along the A-A' profile of Figure 14, crossing the Ionian and continental Greece and the Balkan Mountains. It shows a transition from rather stable ground motions in the Ionian coasts to subsidence (at ~ -1 mm/yr) in continental Greece. Across the Corinth Gulf, subsidence rates are faster (down to -2 mm/yr) and could be associated with the ongoing extensional tectonics of the area. Northward, we find coherent uplift in the Balkans Mountains, up to 1.5 mm/yr. Although the present-day sampling is not dense enough, uplift in Crete could be related to the active shortening and nicely reflects the trend of marine terrace [e.g., Angelier, 1979]. GIA

correction is significant in this zone and reduces in amplitude from south to north, where correction using the ICE-5G model is significantly smaller than KL05.

[72] The B-B' profile of Figure 14 is roughly normal to the Dead Sea valley and shows a steep gradient of ~ 2.5 mm/yr in 40 km with a transition from slow uplift (at ~ -0.5 mm/yr) to fast uplift, with rates up to 2.5 mm/yr, west of the Dead Sea valley, where the highest topography is present. Here GIA is close to zero using both ICE-5G and KL05 models.

[73] Recent studies of the Israel coastal plain suggest a very slow uplift rate of ~ 48 mm/kyr at geological (last 125 ka and since MIS 5e) [Galili *et al.*, 2007; Ronen *et al.*, 2007] and archeological timescales [Anzidei *et al.*, 2011]. Mount Carmel shows average maximum uplift rates of ~ 0.06 mm/yr [Zviely *et al.*, 2009]. The coast of northern Lebanon reveals faster uplift than the rest of the Levantine coasts during late Holocene [Morhange *et al.*, 2006]. However, the geodetic vertical velocities appear sensibly faster than from Holocene and upper Pleistocene data. Conversely, very fast uplift is recognized along growing salt dome at Mount Sedom along the Dead Sea, occurring at ~ 5 – 8 mm/yr, probably at a stable rate over the last 14 ka [Weinberger *et al.*, 2006]. Similar rates have been found using interferometric synthetic aperture radar and GPS over the entire northern Dead Sea, with maximum uplift rates of ~ 4 mm/yr along the northeast coast of the Dead Sea [Nof *et al.*, 2012]. Our vertical velocity field is in agreement with the Nof *et al.* [2012] results, suggesting a correlation with topography, and an increasing rate of uplift moving toward the Dead Sea coasts, suggesting that high rates could be related to elastic unloading due to water level reduction in the lake.

7. Conclusions

[74] We have presented the first synoptic view of contemporary vertical ground velocities in the Euro-Mediterranean region from the analysis of position time series of >800 cGPS stations. Although inherently spatially heterogeneous, due to the distribution of the available networks, the large number of stations in our geodetic solution allows us to highlight coherent patterns of vertical ground motion trends, showing velocity gradients at different spatial scales along the Africa-Eurasia plate-boundary in southern Europe.

[75] The PCA method has proved to be an effective tool to estimate the CME at continental scale, even dealing with highly heterogeneous networks and data continuity through time. The CME in the study region is not a very long wavelength common pattern and it is contained within the first three PCs, which explain $>50\%$ of the total variance. Space-time filtering of position time series with the results of the PCA significantly improves the signal-to-noise ratio, with an $\sim 30\%$ reduction of the WRMS in the vertical component. We have studied and compared stochastic noise processes in position time series and found a mean spectral index of ~ -0.7 from both unfiltered and filtered time series; thus, we have adopted a PL + WN stochastic model in estimating vertical velocities and uncertainties; the latter from filtered time series are $\sim 40\%$ smaller than from the unfiltered ones. A significant reduction of the PL noise component in the filtered time series suggests that colored noise is spatially coherent and forms most of the CME. The WN component,

on the contrary, is of local origin and site specific, and therefore remains unchanged after the space-time filtering.

[76] Our solution highlights new features of the vertical velocity field, which have important implications for geodynamics, tectonics, and sea level studies. In order to provide a rough estimate of the uncertainties associated with the GIA component of the vertical velocity, we have used two different models (ICE-G5 and KL05) in making predictions at each GPS site. Both models provide a similar smooth long wavelength pattern of subsidence over the Mediterranean region, but predictions from the two models differ up to ~0.5 mm/yr in the bulk of the Mediterranean Sea. Correcting the vertical GPS rates for GIA does not significantly change the velocity patterns, and generally, it results in a reduction of the observed subsidence rates and increases of uplift rates, which is particularly evident along peninsular Italy.

[77] The most striking features of the vertical velocity field are apparent plotting rates along cross sections and analyzing the average motion trends. Since vertical velocities are not as coherent at the submillimeter/yr level as the horizontal components, due to the many global and local processes that may affect their motions and uncertainties, our conclusions are stronger where average patterns are observable due to a higher density of data, as in the western and central Mediterranean. New evidences of velocity gradients occurring at both long (>300 km) and shorter spatial scales are shown in Iberia, along the Alps, and the Apennines. In the eastern Mediterranean, the number of sites in our solution is still rather limited and future densifications will be necessary to confirm our preliminary results.

[78] One important finding of our work is the evidence of significant vertical velocity gradients in regions characterized by null to low tectonic activity, such as central Iberia and the western Alps, or that can be even greater than horizontal ones, like in the southeastern Alps. In Iberia, it is difficult to reconcile the topographic features with the estimated vertical velocities, and in the Alps and in the Apennines, we find a correlation between geodetic rates and topography. In general, GIA, active tectonics, and other weathering processes (like erosional unloading) are not able to completely explain the vertical rates, and a combination of different geodynamic processes must be used to explain our observations. Excluding areas where localized processes are likely (e.g., Po Plain, Levantine), or where subduction processes may be active (Calabrian and Hellenic arcs), mantle dynamics is the most likely process, but regional mantle modeling is required to better understand this.

[79] The availability of denser cGPS networks and a more homogeneous distribution of sites over the Euro-Mediterranean in the near future, established in the framework of the European Plate Observing System initiative, will allow improvements of the results presented here.

[80] **Acknowledgments.** We are thankful to all individuals and institutions contributing with GPS data (Table S1) and SOPAC for making available global solutions. We thank Stelios Mertikas (Technical University of Crete) for data of the Gavdos station. We thank Peng Fang (Scripps Institution of Oceanography, UCSD), Bob King, and Tom Herring (MIT) for help and support with the GAMIT/GLOBK software. Adriano Cavaliere (INGV-Bologna) is thanked for support in maintaining the cGPS data archive at INGV. Comments from the Editor (Tom Parson), an Associate Editor, and two anonymous reviewers significantly improved the quality of the manuscript. This work was partially supported by the SIGRIS and COASTSAT projects, funded by the Italian Space Agency (ASI),

and by the PRIN project “Dinamica dei sistemi morfoclimatici in risposta ai cambiamenti globali e rischi geomorfologici indotti” funded by the Italian Ministry of Education, University and Research. All figures have been created using the Generic Mapping Tools (GMT) software [Wessel and Smith, 1991].

References

- Agnew, D. (1992), The time-domain behaviour of power-law noises, *Geophys. Res. Lett.*, *19*(4), 1–4.
- Altamimi, Z., X. Collilieux, J. Legrand, B. Garayt, and C. Boucher (2007), ITRF2005: A new release of the International Terrestrial Reference Frame based on time series of station positions and Earth orientation parameters, *J. Geophys. Res.*, *112*, B09401, doi:10.1029/2007JB004949.
- Altamimi, Z., X. Collilieux, and L. Métivier (2011), ITRF2008: An improved solution of the International Terrestrial Reference Frame, *J. Geodesy*, *85*(8), 457–473, doi:10.1007/s00190-011-0444-4.
- Angelier, J. (1979), Recent Quaternary tectonics in the Hellenic arc: Examples of geological observations on land, *Tectonophysics*, *52*(1), 267–275.
- Antonoli, F., L. Ferranti, K. Lambeck, S. Kershaw, V. Verrubbi, and G. Dai Pra (2006), Late Pleistocene to Holocene record of changing uplift rates in southern Calabria and northeastern Sicily (southern Italy, Central Mediterranean Sea), *Tectonophysics*, *422*(1–4), 23–40, doi:10.1016/j.tecto.2006.05.003.
- Anzidei, M., F. Antonoli, A. Benini, K. Lambeck, D. Sivan, E. Serpelloni, and P. Stocchi (2011), Sea level change and vertical land movements since the last two millennia along the coasts of southwestern Turkey and Israel, *Quatern. Int.*, *232*(1–2), 13–20, doi:10.1016/j.quaint.2010.05.005.
- Argus, D. F. (2007), Defining the translational velocity of the reference frame of Earth, *Geophys. J. Int.*, *169*(3), 830–838, doi:10.1111/j.1365-246X.2007.03344.x.
- Avallone, A., et al. (2010), The RING network: Improvements to a GPS velocity field in the central Mediterranean, *Ann. Geophys.*, *53*(2), 39–54, doi:10.4401/ag-4549.
- Baldi, P., G. Casula, N. Cenni, F. Loddo, and A. Pesci (2009), GPS-based monitoring of land subsidence in the Po Plain (northern Italy), *Earth Planet. Sc. Lett.*, *288*, 204–212, doi:10.1016/j.epsl.2009.09.023.
- Bassin, C., G. Laske, and G. Masters (2000), Current limits of resolution for surface wave tomography in North America, *Eos Trans. AGU*, *81*, F897.
- Battaglia, M., M. H. Murray, E. Serpelloni, and R. Burgmann (2004), The Adriatic region: An independent microplate within the Africa-Eurasia collision zone, *Geophys. Res. Lett.*, *31*, L09605, doi:10.1029/2004GL019723.
- Becker, M., et al. (2002), Assessment of height variations by GPS at Mediterranean and Black Sea coast tide gauges from the SELF projects, *Global Planet. Change*, *34*, 5–35.
- Bennett, R., and S. Hreinsdóttir (2007), Constraints on vertical crustal motion for long baselines in the central Mediterranean region using continuous GPS, *Earth Planet. Sc. Lett.*, *257*(3–4), 419–434, doi:10.1016/j.epsl.2007.03.008.
- Bennett, R. A., S. Hreinsdóttir, M. S. Velasco, and N. P. Fay (2007), GPS constraints on vertical crustal motion in the northern Basin and Range, *Geophys. Res. Lett.*, *34*, L22319, doi:10.1029/2007GL031515.
- Bennett, R. A., et al. (2012), Syn-convergent extension observed using the RETREAT GPS network, northern Apennines, Italy, *J. Geophys. Res.*, *117*, B04408, doi:10.1029/2011JB008744.
- Bertotti, G., R. Capozzi, and V. Picotti (1997), Extension controls quaternary tectonics, geomorphology and sedimentation of the N-Apennines foothills and adjacent Po Plain (Italy), *Tectonophysics*, *282*(1–4), 291–301, doi:10.1016/S0040-1951(97)00229-1.
- Bitelli, G., F. Bonsignore, and M. Unguendoli (2000), Levelling and GPS networks to monitor ground subsidence in the southern Po Valley, *J. Geodyn.*, *30*(3), 355–369.
- von Blanckenburg, F., and J. H. Davies (1995), Slab breakoff: A model for syn-collisional magmatism and tectonics in the Alps, *Tectonics*, *14*, 120–131.
- Blewitt, G., and D. Lavallee (2002), Effect of annual signals on geodetic velocity, *J. Geophys. Res.*, *107*(B7), 2145, doi:10.1029/2001JB000570.
- Boehm, J., and H. Schuh (2004), Vienna mapping functions in VLBI analyses, *Geophys. Res. Lett.*, *31*, L01603, doi:10.1029/2003GL018984.
- Boehm, J., A. Niell, P. Tregoning, and H. Schuh (2006), Global Mapping Function (GMF): A new empirical mapping function based on numerical weather model data, *Geophys. Res. Lett.*, *33*, L07304, doi:10.1029/2005GL025546.
- Bonaccorso, A., A. Bonforte, F. Guglielmino, M. Palano, and G. Puglisi (2006), Composite ground deformation pattern forerunning the 2004–2005 Mount Etna eruption, *J. Geophys. Res.*, *111*, B12207, doi:10.1029/2005JB004206.
- Bos, M. S., R. M. S. Fernandes, S. D. P. Williams, and L. Bastos (2007), Fast error analysis of continuous GPS observations, *J. Geodesy*, *82*(3), 157–166, doi:10.1007/s00190-007-0165-x.
- Bos, M. S., L. Bastos, and R. M. S. Fernandes (2009), The influence of seasonal signals on the estimation of the tectonic motion in short continuous GPS time series, *J. Geodyn.*, *49*(3), 205–209, doi:10.1016/j.jog.2009.10.005.

- Boschi, L., C. Faccenna, and T. W. Becker (2010), Mantle structure and dynamic topography in the Mediterranean Basin, *Geophys. Res. Lett.*, *37*, L20303, doi:10.1029/2010GL045001.
- Bouin, M. N., and G. Wöppelmann (2010), Land motion estimates from GPS at tide gauges: A geophysical evaluation, *Geophys. J. Int.*, *180*(1), 193–209, doi:10.1111/j.1365-246X.2009.04411.x.
- Brighenti, G., P. Macini, and E. Mesini (1998), Subsidence in northern Italy: Compaction measurements of water–gas bearing formations, Proceedings 8th IAGEG Congress, Vancouver: 21–25 September 1998, pp. 207–214.
- Buble, G., R. A. Bennett, and S. Hreinsdóttir (2010), Tide gauge and GPS measurements of crustal motion and sea level rise along the eastern margin of Adria, *J. Geophys. Res.*, *115*, B02404, doi:10.1029/2008JB006155.
- Buiter, S. J. H., R. Govers, and M. Wortel (2002), Two-dimensional simulations of surface deformation caused by slab detachment, *Tectonophysics*, *354*(3), 195–210.
- Carminati, E., and G. Martinelli (2002), Subsidence rates in the Po plain, northern Italy: The relative impact of natural and anthropogenic causation, *Engineering Geology*, *66*(3), 241–255.
- Carminati, E., G. Martinelli, and P. Severi (2003a), Influence of glacial cycles and tectonics on natural subsidence in the Po Plain (northern Italy): Insights from ^{14}C ages, *Geochem. Geophys. Geosyst.*, *4*(10), 1082, doi:10.1029/2002GC000481.
- Carminati, E., C. Dogliani, and D. Scrocca (2003b), Apennines subduction-related subsidence of Venice (Italy), *Geophys. Res. Lett.*, *30*(13), 1717, doi:10.1029/2003GL017001.
- Casas-Sainz, A. M., and G. de Vicente (2009), On the tectonic origin of Iberian topography, *Tectonophysics*, *474*, 214–235, doi:10.1016/j.tecto.2009.01.030.
- Champagnac, J. D., P. Molnar, R. S. Anderson, C. Sue, and B. Delacou (2007), Quaternary erosion-induced isostatic rebound in the western Alps, *Geology*, *35*, 195–198, doi:10.1130/G23053A.1.
- Champagnac, J. D., F. Schlunegger, K. Norton, F. von Blanckenburg, L. M. Abbühl, and M. Schwab (2009), Erosion-driven uplift of the modern Central Alps, *Tectonophysics*, *474*, 236–249, doi:10.1016/j.tecto.2009.02.024.
- Church, J. A., J. M. Gregory, P. Huybrechts, M. Kuhn, K. Lambeck, M. T. Nhan, D. Qin, and P. L. Woodworth (2001), Changes in sea level, in *Climate Change 2001: The Scientific Basis. Contribution of Working Group I to the Third Assessment Report of the Intergovernmental Panel on Climate Change*, edited by J. T. Houghton et al., pp. 639–694, Cambridge Univ. Press, Cambridge, U.K.
- Cloetingh, S., E. Burov, F. Beekman, B. Andeweg, P. Andriessen, D. Garcia-Castellanos, V. Muñoz, and R. Vegas (2002), Lithospheric folding in Iberia, *Tectonics*, *21*(5), 1041, doi:10.1029/2001TC901031.
- D'Agostino, N., J. A. Jackson, F. Dramis, and R. Funicello (2001), Interactions between mantle upwelling, drainage evolution and active normal faulting: An example from the central Apennines (Italy), *Geophys. J. Int.*, *147*, 475–497.
- D'Agostino, N., D. Cheloni, S. Mantenuto, G. Selvaggi, A. Michelini, and D. Zuliani (2005), Strain accumulation in the southern Alps (NE Italy) and deformation at the northeastern boundary of Adria observed by cGPS measurements, *Geophys. Res. Lett.*, *32*, L19306, doi:10.1029/2005GL024266.
- D'Anastasio, E., P. M. De Martini, G. Selvaggi, D. Pantosti, A. Marchioni, and R. Maseroli (2006), Short-term vertical velocity field in the Apennines (Italy) revealed by geodetic levelling data, *Tectonophysics*, *418*(3–4), 219–234, doi:10.1016/j.tecto.2006.02.008.
- Dávila, F. M., C. Lithgow-Bertelloni, and M. Giménez (2010), Tectonic and dynamic controls on the topography and subsidence of the Argentine Pampas: The role of the flat slab, *Earth Planet. Sci. Lett.*, *295*(1–2), 187–194, doi:10.1016/j.epsl.2010.03.039.
- De Vicente, G., et al. (2007), Cenozoic thick-skinned deformation and topography evolution of the Spanish Central System, *Global Planet. Change*, *58*, 335–381.
- Devoti, R., G. Pietrantonio, A. Pisani, F. Riguzzi, and E. Serpelloni (2010), Present day kinematics of Italy, in *The Geology of Italy: Tectonics and Life Along Plate Margins. J. Virtual Explorer*, Electronic Ed., vol. 36, edited by M. Beltrando et al., paper 2, doi:10.3809/jvirtex.2009.00237.
- Devoti, R., A. Esposito, G. Pietrantonio, A. R. Pisani, and F. Riguzzi (2011), Evidence of large scale deformation patterns from GPS data in the Italian subduction boundary, *Earth Planet. Sci. Lett.*, *311*(3–4), 1–12, doi:10.1016/j.epsl.2011.09.034.
- Devoti, R., L. Anderlini, M. Anzidei, A. Esposito, A. Galvani, G. Pietrantonio, A. R. Pisani, F. Riguzzi, V. Sepe, and E. Serpelloni (2012), The coseismic and postseismic deformation of the L'Aquila, 2009 earthquake from repeated GPS measurements, *Ital. J. Geosci. (Boll. Soc. Geol. It.)*, *131*(3), 348–358, doi:10.3301/IJG.2012.15.
- Dong, D., T. Herring, and R. King (1998), Estimating regional deformation from a combination of space and terrestrial geodetic data, *J. Geodesy*, *72*(4), 200–214.
- Dong, D., P. Fang, Y. Bock, M. Cheng, and S. Miyazaki (2002), Anatomy of apparent seasonal variations from GPS-derived site position time series, *J. Geophys. Res.*, *107*(B4), 2075, doi:10.1029/2001JB000573.
- Dong, D., P. Fang, Y. Bock, F. Webb, L. Prawirodirdjo, S. Kedar, and P. Jamason (2006), Spatiotemporal filtering using principal component analysis and Karhunen-Loeve expansion approaches for regional GPS network analysis, *J. Geophys. Res.*, *111*, B03405, doi:10.1029/2005JB003806.
- Faccenna, C., and T. W. Becker (2010), Shaping mobile belts by small-scale convection, *Nature*, *465*(7298), 602–605, doi:10.1038/nature09064.
- Faccenna, C., P. Molin, B. Orecchio, V. Olivetti, O. Bellier, F. Funicello, L. Minelli, C. Piromallo, and A. Billi (2011), Topography of the Calabria subduction zone (southern Italy): Clues for the origin of Mt. Etna, *Tectonics*, *30*, TC1003, doi:10.1029/2010TC002694.
- Farrell, W. E., and J. A. Clark (1976), On postglacial sea level, *Geophys. J. R. Astron. Soc.*, *46*, 647–667, doi:10.1111/j.1365-246X.1976.tb01252.x.
- Fay, N. P., R. A. Bennett, and S. Hreinsdóttir (2008), Contemporary vertical velocity of the central Basin and Range and uplift of the southern Sierra Nevada, *Geophys. Res. Lett.*, *35*, L20309, doi:10.1029/2008GL034949.
- Fernández, M., I. Marzán, A. Correia, and E. Ramalho (1998), Heat flow, heat production, and lithospheric thermal regime in the Iberian Peninsula, *Tectonophysics*, *291*, 29–53.
- Ferranti, L., et al. (2006), Markers of the last interglacial sea-level high stand along the coast of Italy: Tectonic implications, *Quatern. Int.*, *145–146*, 30–54, doi:10.1016/j.quaint.2005.07.009.
- Floyd, M. A., et al. (2010), A new velocity field for Greece: Implications for the kinematics and dynamics of the Aegean, *J. Geophys. Res.*, *115*, B10403, doi:10.1029/2009JB007040.
- Gallili, E., D. Zviely, A. Ronen, and H. K. Mienis (2007), Beach deposits of MIS 5e high sea stand as indicators for tectonic stability of the Carmel coastal plain, Israel, *Quat. Sci. Rev.*, *26*(19–21), 2544–2557, doi:10.1016/j.quascirev.2007.06.027.
- Ganas, A., E. Serpelloni, G. Drakatos, M. Kolligri, I. Adamis, C. Tsimi, and E. Batsi (2009), The M_w 6.4 SW-Achaia (western Greece) earthquake of 8 June 2008: Seismological, field, GPS observations, and stress modeling, *J. Earthq. Eng.*, *13*(8), 1101–1124, doi:10.1080/13632460902933899.
- García-Castellanos, D., J. Vergés, J. Gaspar-Escribano, and S. Cloetingh (2003), Interplay between tectonics, climate, and fluvial transport during the Cenozoic evolution of the Ebro Basin (NE Iberia), *J. Geophys. Res.*, *108*(B7), 2347, doi:10.1029/2002JB002073.
- Gerya, T. V., D. A. Yuen, and W. V. Maresch (2004), Thermomechanical modelling of slab detachment, *Earth Planet. Sci. Lett.*, *226*(1–2), 101–116, doi:10.1016/j.epsl.2004.07.022.
- Giacomuzzi, G., C. Chiarabba, and P. De Gori (2011), Linking the Alps and Apennines subduction systems: New constraints revealed by high-resolution teleseismic tomography, *Earth Planet. Sci. Lett.*, *301*(3–4), 531–543, doi:10.1016/j.epsl.2010.11.033.
- Giambastiani, B. M. S., M. Antonellini, G. H. P. Oude Essink, and R. J. Stuurman (2007), Saltwater intrusion in the unconfined coastal aquifer of Ravenna (Italy): A numerical model, *J. Hydrol.*, *340*, 91–104.
- Gurnis, M. (1992), Rapid continental subsidence following the initiation and evolution of subduction, *Science*, *255*, 1556–1558.
- Herring, T., R. W. King, and S. McClusky (2010), *GAMIT Reference Manual, Release 10.4*, Massachusetts Institute of Technology, Cambridge, MA.
- Hunstad, I., G. Selvaggi, N. D'Agostino, P. England, P. Clarke, and M. Pierozzi (2003), Geodetic strain in peninsular Italy between 1875 and 2001, *Geophys. Res. Lett.*, *30*(4), 1181, doi:10.1029/2002GL016447.
- Husson, L. (2006), Dynamic topography above retreating subduction zones, *Geology*, *34*(9), 741–744.
- Husson, L., B. Guillaume, F. Funicello, C. Faccenna, and L. H. Royden (2012), Unraveling topography around subduction zones from laboratory models, *Tectonophysics*, *526–529*, 5–15, ISSN 0040–1951, doi:10.1016/j.tecto.2011.09.001.
- Johansson, J. M., et al. (2002), Continuous GPS measurements of postglacial adjustment in Fennoscandia—I. Geodetic results, *J. Geophys. Res.*, *107*, doi:10.1029/2001JB000400.
- Kaniuth, K., and S. Vetter (2005), Vertical velocities of European coastal sites derived from continuous GPS observations, *GPS Solut.*, *9*(1), 32–40, doi:10.1007/s10291-004-0124-4.
- Kierulf, H. P., et al. (2008), Comparison of GPS analysis strategies for high-accuracy vertical land motion, *Phys. Chem. Earth*, *33*, 194–204, doi:10.1016/j.pce.2006.11.003.
- King, M. A., and S. D. P. Williams (2009), Apparent stability of GPS monumentation from short-baseline time series, *J. Geophys. Res.*, *114*, B10403, doi:10.1029/2009JB006319.
- King, M. A., M. Bevis, T. Wilson, B. Johns, and F. Blume (2012), Monument-antenna effects on GPS coordinate time-series with application to vertical rates in Antarctica, *J. Geodesy*, *86*(1), 53–63, doi:10.1007/s00190-011-0491-x.

- Lambeck, K., and A. Purcell (2005), Sea-level change in the Mediterranean Sea since the LGM: Model predictions for tectonically stable areas, *Quat. Sci. Rev.*, *24*(18–19), 1969–1988, doi:10.1016/j.quascirev.2004.06.025.
- Lambeck, K., C. Smither, and P. Johnston (1998), Sea-level change, glacial rebound and mantle viscosity for northern Europe, *Geophys. J. Int.*, *134*, 102–144, doi:10.1046/j.1365-246x.1998.00541.x.
- Langbein, J., and H. Johnson (1997), Correlated errors in geodetic time series: Implications for time-dependent deformation, *J. Geophys. Res.*, *102*, 591–603.
- Lippitsch, R., E. Kissling, and J. Ansorge (2003), Upper mantle structure beneath the Alpine orogen from high-resolution teleseismic tomography, *J. Geophys. Res.*, *108*(B8), 2376, doi:10.1029/2002JB002016.
- Lombardi, D., J. Braummiller, E. Kissling, and D. Giardini (2008), Moho depth and Poisson's ratio in the western-central Alps from receiver functions, *Geophys. J. Int.*, *173*, 249–264, doi:10.1111/j.1365-246X.2007.03706.x.
- Lyard, F., F. Lefevre, T. Letellier, and O. Francis (2006), Modelling the global ocean tides: Modern insights from FES2004, *Ocean Dynam.*, *56*, 394–415.
- Mao, A., C. Harrison, and T. Dixon (1999), Noise in GPS coordinate time series, *J. Geophys. Res.*, *104*(B2), 2797–2816.
- Marquez-Azua, B., and C. DeMets (2003), Crustal velocity field of Mexico from continuous GPS measurements, 1993 to June 2001: Implications for the neotectonics of Mexico, *J. Geophys. Res.*, *108*(B9), 2450, doi:10.1029/2002JB002241.
- Mele, G., A. Rovelli, D. Seber, and M. Barazangi (1997), Shear wave attenuation in the lithosphere beneath Italy and surrounding regions: Tectonic implications, *J. Geophys. Res.*, *102*(B6), 11,863–11,875, doi:10.1029/97JB00262.
- Milne, G. A., and J. X. Mitrovica (1998), Postglacial sea-level change on a rotating Earth, *Geophys. J. Int.*, *133*, 1–19, doi:10.1046/j.1365-246X.1998.1331455.x.
- Mitrovica, J. X., C. Beaumont, and G. T. Jarvis (1989), Tilting of continental interiors by the dynamical effects of subduction, *Tectonics*, *8*(5), 1079–1094.
- Miyauchi, T., G. Dai Pra, and S. Sylos Labini (1994), Geochronology of Pleistocene marine terraces and regional tectonics in the Tyrrhenian coast of South Calabria, Italy, *Il Quaternario*, *7*, 17–34.
- Molnar, P., and P. England (1990), Late Cenozoic uplift of mountain-ranges and global climate change—Chicken or egg, *Nature*, *346*, 29–34.
- Morhange, C., P. A. Pirazzoli, N. Marriner, L. F. Montaggioni, and T. Nammour (2006), Late Holocene relative sea-level changes in Lebanon, Eastern Mediterranean, *Mar. Geol.*, *230*(1–2), 99–114, doi:10.1016/j.margeo.2006.04.003.
- Nocquet, J. M., and E. Calais (2004), Geodetic measurements of crustal deformation in the Western Mediterranean and Europe, *Pure Appl. Geophys.*, *161*(3), 661–681.
- Nocquet, J. M., E. Calais, and B. Parsons (2005), Geodetic constraints on glacial isostatic adjustment in Europe, *Geophys. Res. Lett.*, *32*, L06308, doi:10.1029/2004GL022174.
- Nof, R. N., A. Ziv, M. P. Doin, G. Baer, Y. Fialko, S. Wdowinski, Y. Eyal, and Y. Bock (2012), Rising of the lowest place on Earth due to Dead Sea water-level drop: Evidence from SAR interferometry and GPS, *J. Geophys. Res.*, *117*, B05412, doi:10.1029/2011JB008961.
- Ostanciaux, É., L. Husson, G. Choblet, C. Robin, and K. Pedoja (2012), Present-day trends of vertical ground motion along the coast lines, *Earth Sci. Rev.*, *110*(1–4), 74–92, doi:10.1016/j.earscirev.2011.10.004.
- Peltier, W. R. (2004), Global glacial isostasy and the surface of the ice-age Earth: The ICE-5G (VM2) model and GRACE, *Annu. Rev. Earth Planet. Sci.*, *32*(1), 111–149, doi:10.1146/annurev.earth.32.082503.144359.
- Petrie, E. J., M. A. King, P. Moore, and D. A. Lavallée (2010), Higher-order ionospheric effects on the GPS reference frame and velocities, *J. Geophys. Res.*, *115*, B03417, doi:10.1029/2009JB006677.
- Pezzo, G., et al. (2013), Coseismic deformation and source modeling of the May 2012 Emilia (northern Italy) earthquakes, *Seismol. Res. Lett.*, *84*(4), 645–655, doi:10.1785/0220120171.
- Piana Agostinetti, N., and A. Amato (2009), Moho depth and Vp/Vs ratio in peninsular Italy from teleseismic receiver functions, *J. Geophys. Res.*, *114*, B06303, doi:10.1029/2008JB005899.
- Picotti, V., and F. J. Pazzaglia (2008), A new active tectonic model for the construction of the Northern Apennines mountain front near Bologna (Italy), *J. Geophys. Res.*, *113*, B08412, doi:10.1029/2007JB005307.
- Piomallo, C., and C. Faccenna (2004), How deep can we find the traces of Alpine subduction?, *Geophys. Res. Lett.*, *31*, L06605, doi:10.1029/2003GL019288.
- Piomallo, C., and A. Morelli (2003), P-wave tomography of the mantle under the Alpine-Mediterranean area, *J. Geophys. Res.*, *108*(B2), 2065, doi:10.1029/2002JB001757.
- Ronen, A., D. Zviely, and E. Galili (2007), Did the last interglacial sea penetrate Mount Carmel caves? Comments on “The setting of the Mt. Carmel caves reassessed” by C. Vita-Finzi and C. Stringer, *Quat. Sci. Rev.*, *26*(19–21), 2684–2685, doi:10.1016/j.quascirev.2007.06.003.
- Santamaría-Gómez, A., M. N. Bouin, X. Collilieux, and G. Wöppelmann (2011), Correlated errors in GPS position time series: Implications for velocity estimates, *J. Geophys. Res.*, *116*, B01405, doi:10.1029/2010JB007701.
- Santamaría-Gómez, A., M. Gravelle, X. Collilieux, M. Guichard, B. Martín Míguez, P. Tiphaneau, and G. Wöppelmann (2012), Mitigating the effects of vertical land motion in tide gauge records using a state-of-the-art GPS velocity field, *Global Planet. Change*, Volumes 98–99, 6–17, ISSN 0921–8181, doi:10.1016/j.gloplacha.2012.07.007.
- Schlatter, A., D. Schneider, A. Geiger, and H. G. Kahle (2004), Recent vertical movements from precise levelling in the vicinity of the city of Basel, Switzerland, *Int. J. Earth Sci. (Geol. Rundsch.)*, *94*(4), 507–514, doi:10.1007/s00531-004-0449-9.
- Schmid, R., M. Rothacher, D. Thaller, and P. Steigenberger (2005), Absolute phase center corrections of satellite and receiver antennas, *GPS Solut.*, *9*(4), 283–293, doi:10.1007/s10291-005-0134-x.
- Schmid, R., P. Steigenberger, G. Gendt, M. Ge, and M. Rothacher (2007), Generation of a consistent absolute phase-center correction model for GPS receiver and satellite antennas, *J. Geodesy*, *81*(12), 781–798, doi:10.1007/s00190-007-0148-y.
- Serpelloni, E., M. Anzidei, P. Baldi, G. Casula, and A. Galvani (2005), Crustal velocity and strain-rate fields in Italy and surrounding regions: New results from the analysis of permanent and non-permanent GPS networks, *Geophys. J. Int.*, *161*(3), 861–880, doi:10.1111/j.1365-246X.2005.02618.x.
- Serpelloni, E., G. Casula, A. Galvani, M. Anzidei, and P. Baldi (2006), Data analysis of permanent GPS networks in Italy and surrounding regions: Application of a distributed processing approach, *Ann. Geophys.-Italy*, *49*, 897–928.
- Serpelloni, E., G. Vannucci, S. Pondrelli, A. Argnani, G. Casula, M. Anzidei, P. Baldi, and P. Gasperini (2007), Kinematics of the Western Africa-Eurasia plate boundary from focal mechanisms and GPS data, *Geophys. J. Int.*, *169*(3), 1180–1200, doi:10.1111/j.1365-246X.2007.03367.x.
- Serpelloni, E., R. Bürgmann, M. Anzidei, P. Baldi, B. Mastrolembo Ventura, and E. Boschi (2010), Strain accumulation across the Messina Straits and kinematics of Sicily and Calabria from GPS data and dislocation modeling, *Earth Planet. Sc. Lett.*, *298*(3–4), 347–360, doi:10.1016/j.epsl.2010.08.005.
- Serpelloni, E., L. Anderlini, and M. E. Belardinelli (2012a), Fault geometry, coseismic-slip distribution and Coulomb stress change associated with the 2009 April 6, M_w 6.3, L'Aquila earthquake from inversion of GPS displacements, *Geophys. J. Int.*, doi:10.1111/j.1365-246X.2011.05279.x.
- Serpelloni, E., L. Anderlini, and A. Avallone (2012b), GPS observations of coseismic deformation following the May 20 and 29, 2012, Emilia seismic events (northern Italy): Data, analysis and preliminary models, *Ann. Geophys.*, *55*, 4, doi:10.4401/ag-6168.
- Smith, W. H. F., and P. Wessel (1990), Gridding with continuous curvature splines in tension, *Geophysics*, *55*, 293–305.
- Spada, G., and G. Galassi (2012), New estimates of secular sea level rise from tide gauge data and GIA modelling, *Geophys. J. Int.*, *191*, 1067–1094, doi:10.1111/j.1365-246X.2012.05663.x.
- Spada, G., and P. Stocchi (2007), SELEN: A Fortran 90 program for solving the “sea level equation”, *Comput. and Geosci.*, *33*(4), 538–562, doi:10.1016/j.cageo.2006.08.006.
- Steigenberger, P., M. Rothacher, R. Dietrich, M. Fritsche, A. Rülke, and S. Vey (2006), Reprocessing of a global GPS network, *J. Geophys. Res.*, *111*, B05402, doi:10.1029/2005JB003747.
- Stich, D., E. Serpelloni, F. de Lis Mancilla, and J. Morales (2006), Kinematics of the Iberia–Maghreb plate contact from seismic moment tensors and GPS observations, *Tectonophysics*, *426*(3–4), 295–317, doi:10.1016/j.tecto.2006.08.004.
- Stocchi, P., and G. Spada (2009), Influence of glacial isostatic adjustment upon current sea level variations in the Mediterranean, *Tectonophysics*, *474*(1–2), 56–68, doi:10.1016/j.tecto.2009.01.003.
- Stocchi, P., G. Spada, and S. Cianetti (2005), Isostatic rebound following the Alpine deglaciation: Impact on the sea level variations and vertical movements in the Mediterranean region, *Geophys. J. Int.*, *162*(1), 137–147, doi:10.1111/j.1365-246X.2005.02653.x.
- Stocchi, P., F. Colletti, and G. Spada (2009), Bounds on the time history and Holocene mass budget of Antarctica from sea level records in SE Tunisia, *Pure Appl. Geophys.*, *166*(8–9), 1319–1341, doi:10.1007/s00024-009-0488-z.
- Teatini, P., M. Ferronato, G. Gambolati, and M. Gonella (2006), Groundwater pumping and land subsidence in the Emilia-Romagna coastland, Italy: Modeling the past occurrence and the future trend, *Water Resour. Res.*, *42*, W01406, doi:10.1029/2005WR004242.
- Teferle, F., S. Williams, H. Kierulf, R. Bingley, and H. Plag (2008), A continuous GPS coordinate time series analysis strategy for high-accuracy

- vertical land movements, *Phys. Chem. Earth, Parts A/B/C*, 33(3–4), 205–216, doi:10.1016/j.pce.2006.11.002.
- Tesauro, M., M. K. Kaban, and S. A. P. L. Cloetingh (2008), EuCRUST-07: A new reference model for the European crust, *Geophys. Res. Lett.*, 35, L05313, doi:10.1029/2007GL032244.
- van Dam, T. M., G. Blewitt, and M. B. Heflin (1994), Atmospheric pressure loading effects on global positioning system coordinate determinations, *J. Geophys. Res.*, 99(B12), 23,939–23,950.
- van Dam, T. M., J. Wahr, P. C. D. Milly, A. B. Shmakin, G. Blewitt, D. Lavalley, and K. M. Larson (2001), Crustal displacements due to continental water loading, *Geophys. Res. Lett.*, 28(4), 651–654.
- Wdowinski, S., Y. Bock, J. Zhang, P. Fang, and J. Genrich (1997), Southern California Permanent GPS Geodetic Array: Spatial filtering of daily positions for estimating coseismic and postseismic displacements induced by the 1992 Landers earthquake, *J. Geophys. Res.*, 102(B8), 18,057–18,070.
- Weinberger, R., V. Lyakhovskiy, G. Baer, and Z. B. Begin (2006), Mechanical modeling and InSAR measurements of Mount Sedom uplift, Dead Sea basin: Implications for effective viscosity of rock salt, *Geochem. Geophys. Geosyst.*, 7, Q05014, doi:10.1029/2005GC001185.
- Wessel, P., and W. H. F. Smith (1991), Free software helps map and display data, *EOS Trans. AGU*, 72, 441.
- Westaway, R., and D. Bridgland (2007), Late Cenozoic uplift of southern Italy deduced from fluvial and marine sediments: Coupling between surface processes and lower-crustal flow, *Quat. Int.*, 175(1), 86–124, doi:10.1016/j.quaint.2006.11.015.
- Williams, S. D. P. (2003), The effect of coloured noise on the uncertainties of rates estimated from geodetic time series, *J. Geodesy*, 76, 483–494, doi:10.1007/s00190-002-0283-4.
- Williams, S. D. P. (2008), CATS: GPS coordinate time series analysis software, *GPS Solut.*, 12(2), 147–153, doi:10.1007/s10291-007-0086-4.
- Williams, S. D. P., Y. Bock, P. Fang, P. Jamason, R. Nikolaidis, L. Prawirodirdjo, M. Miller, and D. Johnson (2004), Error analysis of continuous GPS position time series, *J. Geophys. Res.*, 109, B03412, doi:10.1029/2003JB002741.
- Wittmann, H., F. von Blanckenburg, T. Kruesmann, K. P. Norton and P. Kubik (2007), The relation between rock uplift and denudation from cosmogenic nuclides in river sediment in the Central Alps of Switzerland, *J. Geophys. Res.*, 112, F04010, doi:10.1029/2006JF000729.
- Wöppelmann, G., M. N. Bouin, X. Collilieux, Z. Altamimi, and S. D. P. Williams (2009), Rates of sea-level change over the past century in a geocentric reference frame, *Geophys. Res. Lett.*, 36, L12607, doi:10.1029/2009GL038720.
- Wortel, M. J. R., and W. Spakman (2000), Subduction and slab detachment in the Mediterranean-Carpathian region, *Science*, 290, 1910–1917.
- Zviely, D., E. Galili, A. Ronen, A. Salamon, and Z. Ben-Avraham (2009), Reevaluating the tectonic uplift of western Mount Carmel, Israel, since the middle Pleistocene, *Quat. Res.*, 71(2), 239–245, doi:10.1016/j.yqres.2008.11.008.